Effects of Abdomen Undulation in Energy Consumption and Stability for Monarch Butterfly

Tejaswi K. C.[1], **Madhu K. Sridhar**[2], **Chang-kwon Kang**[2] **and Taeyoung Lee**[1]

[1] Mechanical and Aerospace Engineering, The George Washington University, Washington DC 20052
[2] Mechanical and Aerospace Engineering, University of Alabama in Huntsville, Huntsville AL 35899

E-mail: tylee@gwu.edu

Abstract. The flight of monarch butterflies is characterized by a relatively large wing, flapping at a relatively low frequency coupled with abdomen undulation. This paper presents the dynamics of a flapping wing flyer that can be applied to the coupled motion of the wing, body, and abdomen at the monarch butterfly scale, which is formulated directly on the configuration manifold. The resulting thorax and abdomen motion as well as the resultant forces are consistent with the flight of a live monarch butterfly. Based on these, beneficial effects of the abdomen undulation in the flight of monarch butterflies are illustrated. For both hover and forward-climbing trajectories, the abdomen undulation results in a reduction of the energy and power consumption. Furthermore, the Floquet stability analysis shows that the periodic orbits associated with both flight modes are stable. In particular, the abdomen undulation improves the stability. Compared to the dynamics of hawkmoth, bumblebee, and fruitfly models, the monarch possesses superior stability properties.

Keywords: insect flight, abdomen, energy consumption, dynamics and stability

Submitted to: *Bioinspir. Biomim.*

1. Introduction

The monarch butterfly is one of the most popular butterfly species in North America with wing lengths of around $4\,\mathrm{cm}$. They exhibit remarkable flight characteristics [1], migrating annually from North America to Mexico - up to $4000\,\mathrm{km}$ [2–4], the longest flight range among insects [2, 5–7]. An accurate model of the butterfly dynamics can contribute to our understanding of the long-range monarch migration. This, in turn, can potentially inform the development of long-range micro flying robots. However, the physical mechanism enabling this long-range flight is not well understood yet.

Compared to the wealth of research on the flight of insects such as flies [8, 9], bees [10, 11], dragonflies [12–16], or birds and bats [17], butterfly flight remains inadequately understood due to their many unique characteristics. Unlike most insects, the fore and hindwings of butterflies are relatively large and move in sync [18]. Butterflies are extremely evasive with agile maneuvers [19–22] and body undulations with closely coupled wing-body interaction [21, 23, 24]. The butterfly body exhibits considerable vertical oscillation during

flight due to the instantaneous change in wing shape and inertia [23, 25], resulting in a bumpy flight trajectory.

The main obstacle in discovering the long-range flight mechanisms in the monarch flight is this highly coupled dynamics of the slowly flapping motion and the body. The large wings continuously rotate during flight, which is also affected by the body dynamics. Furthermore, the thorax of the monarchs continuously pitches while their abdomen moves relative to the thorax during flight. As a consequence, most flight dynamic equations of motion and control schemes that have been derived in the literature cannot be used to study the butterfly flight. More specifically, the conventional models exploit the large disparity in the time scales of wingbeat frequency and body dynamics assuming smaller insects such as fruit flies and bumblebees [26, 27]. Furthermore, many flapping wing dynamics models are based on the common simplified formulation where the nonlinear time-varying flapping dynamics are transformed into linear time-invariant systems by considering small perturbations averaged over the period of flapping [28–31]. These approaches are not suitable to analyze the low-frequency flapping dynamics of monarch butterflies.

There are several key open research questions associated with the effects of dynamics on the butterfly flight. Whereas the pitching motion of smaller flying insects play a critical role in aerodynamic force generation [8, 17], most butterfly wings are structurally restricted from pitching [25]. It is presumed that the body attitude and vertical displacement benefits the aerodynamic force generation. A simple flapping wing motions affects the body dynamics, which alter the effective angle of attack and, hence, the flapping wing aerodynamics. This mechanism was illustrated by an experiment involving a simple flapping butterfly inspired ornithopter without a tail, which could fly forward passively without a feedback controller by adjusting the center of mass [25]. However, there are also reports that contradict these findings and beneficial effects. Flight of model butterflies was shown to be unstable under periodic flapping motion, because the body pitch angle diverged [32, 33]. The motion of the abdomen had to be actively controlled to stabilize the butterfly flight [33]. Furthermore, the abdominal undulation can potentially redirect lift forces for effective flight control [34]. However, the effects of the abdominal undulation on the energy consumption and stability are unknown.

The objective of this paper is to derive, validate, and analyze a dynamic model that can characterize the monarch butterfly flight. Here, we focus on the question if the abdominal motion relative to the thorax can save power or enhance stability. We also test the hypothesis if the undulating motion of the abdomen can be purely passive. If the mechanism enabling the forward flight of butterflies is passive, or partly passive, the power consumption is expected to be lower than an actively controlled flight.

To answer these questions, we model a flapping wing flyer as articulated rigid bodies, where two wings and an abdomen are connected to a thorax via spherical joints. An intrinsic form of Lagrangian mechanics is developed to include and study the inertial effects of the relative rotation between each part. These are developed on the nonlinear configuration manifold in a global fashion such that large angle rotational maneuvers can be analyzed without singularities and ambiguities inherent to the common attitude parameterizations. Further, the resulting elegant, structured form of the equations of motion can be easily utilized in stability analysis and controller design.

To model the flapping wing aerodynamics, a quasi-steady blade element model is formulated without relying on the common assumption that the flapping frequency is sufficiently large. For the butterfly flight, the aerodynamic forces generated by the wing vary along the spanwise direction as the velocity generated by the flapping is comparable to the velocity of the thorax. We find the expression for the angle of attack at each infinitesimal

chord of the wing as a function of the wing kinematics and the rotation and translation of the body, which is then utilized to compute the aerodynamic forces and moments. In short, the proposed dynamic model captures the unique characteristics of the butterfly flight dynamics where the flapping of large wings are coupled with the thorax and the abdomen undulation. More specifically, it can represent the effects of the mass distribution of the relatively large wing, the inertial coupling with the abdomen undulation, and the low frequency flapping aerodynamics coupled with the body motion. The live monarch butterfly flight is measured using a motion-tracking system [24], and the corresponding wing kinematics and the body undulations are extracted.

Next, based on the proposed dynamic model of butterflies, we compute a particular wing kinematics and body/abdomen undulation required to complete a specific flight maneuver, namely hovering flight and forward-climbing flight. It is formulated as an optimization problem to satisfy constraints required for the selected maneuver, while minimizing a performance index characterizing energy and power consumption.

Finally, we analyze the stability of periodic orbits constructed above utilizing the Floquet theory [35]. After analyzing the effects of abdomen undulation on stability, the stability of the live monarch butterfly flight is discussed. These are further compared against other insects with varying flapping frequencies and wing sizes.

In short, the main contributions of this paper are threefold: proposing a new dynamic model that can characterize the unique properties of butterfly, analyzing the flight dynamics of live monarch butterfly, and characterizing the beneficial effects of abdomen undulation in energy and stability.

2. Dynamics of Flapping-Wing Flyer

In this section, we present a dynamic model of a flapping-wing unmanned aerial vehicle that can characterize the flight of monarch butterflies, where wing flapping motion is coupled with abdomen undulation. The standard notations utilized in this paper are listed here for convenience. First, $\mathsf{SO(3)} = \{R \in \mathbb{R}^{3\times 3} \mid R^T R = I, \det(R) = 1\}$ denotes the rotation group in three dimensions, and $\mathfrak{so}(3) = \{A \in \mathbb{R}^{3\times 3} \mid A = -A^T\}$ is the corresponding Lie algebra. Define the *hat* map $\wedge : \mathbb{R}^3 \to \mathfrak{so}(3)$ as $\hat{x}y = x \times y$ for any $x, y \in \mathbb{R}^3$, along with its inverse the *vee* map, $\vee : \mathfrak{so}(3) \to \mathbb{R}^3$. Next, the n-dimensional i-th standard basis of $\mathbb{R}^n$ is represented by $e_i \in \mathbb{R}^n$, for instance, $e_1 = (1, 0, \ldots, 0) \in \mathbb{R}^n$. Moreover, all the units used are in SI, e.g., kg, m, s, and rad, unless specified otherwise. Furthermore, for a three dimensional Euclidean vector, v, its 1st component v_1 corresponds to the x-axis, 2nd component v_2 to the y-axis and the 3rd component v_3 to the z-axis.

Full derivation and details of this model are lengthy and presented in the online supplementary material. The morphological parameters along with the inertial properties of real butterflies which are used as input for the results presented in the later sections can be found in the online supplementary material.

2.1. Flapping Wing Kinematics

The articulated rigid body model of a flapping wing flyer consists of a body, an abdomen, and two wings attached to the body. Here, the body refers to a single rigid body which integrates the head and the thorax. Also, we do not distinguish hindwings from forewings.

An inertial frame $\mathcal{F}_I = \{\mathbf{i}_x, \mathbf{i}_y, \mathbf{i}_z\}$ is defined, which is compatible to the standard NED (north-east-down) frame in flight mechanics. The various components of the model relative to this frame are the body, right wing, left wing, and abdomen.

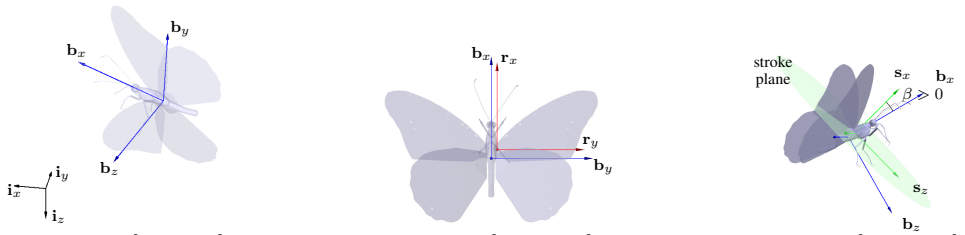

(a) $\mathcal{F}_I = \{\mathbf{i}_x, \mathbf{i}_y, \mathbf{i}_z\}$; $\mathcal{F}_B = \{\mathbf{b}_x, \mathbf{b}_y, \mathbf{b}_z\}$ (b) $\mathcal{F}_R = \{\mathbf{r}_x, \mathbf{r}_y, \mathbf{r}_z\}$ (c) $\mathcal{F}_S = \{\mathbf{s}_x, \mathbf{s}_y, \mathbf{s}_z\}$

Figure 1. Inertial frame, body fixed frame, wing frame and the stroke frame.

For the body (head/thorax), a body-fixed frame $\mathcal{F}_B = \{\mathbf{b}_x, \mathbf{b}_y, \mathbf{b}_z\}$ (fig. 1.(a)) is attached at center of mass of the body which is located at $x \in \mathbb{R}^3$ in $\mathcal{F}_I$. The kinematics of its attitude, $R \in \mathsf{SO}(3)$, is

$$\dot{R} = R\hat{\Omega}, \tag{1}$$

where $\Omega \in \mathbb{R}^3$ is its angular velocity resolved in the body-fixed frame.

The motion of the right wing is described in a frame $\mathcal{F}_R = \{\mathbf{r}_x, \mathbf{r}_y, \mathbf{r}_z\}$ (fig. 1.(b)), attached to the right wing root. The stroke frame, $\mathcal{F}_S = \{\mathbf{s}_x, \mathbf{s}_y, \mathbf{s}_z\}$ (fig. 1.(c)), is obtained by translating $\mathcal{F}_B$ to the center of wing roots, and rotating it about $\mathbf{b}_y$ by the stroke angle, β. Denote the fixed vector joining the origins of $\mathcal{F}_B$ and $\mathcal{F}_R$ as $\mu_R \in \mathbb{R}^3$.

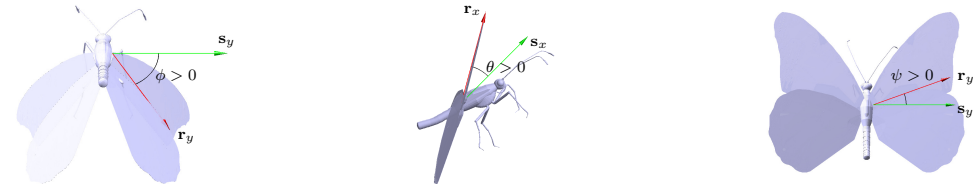

(a) flapping angle, $\phi_R \in [-\pi, \pi)$ (b) pitch angle, $\theta_R \in [-\pi, \pi)$ (c) deviation angle, $\psi_R \in [-\pi, \pi)$

Figure 2. Euler angles: positive values are indicated from $\mathcal{F}_S$ (green) to $\mathcal{F}_R$ (red).

Let $Q_R \in \mathsf{SO}(3)$ be the attitude of the right wing relative to $\mathcal{F}_S$. It can be represented by the combination of 1–3–2 Euler angles $(\phi_R(t), \psi_R(t), \theta_R(t))$ as

$$Q_R = \exp(\beta\hat{e}_2)\exp(\phi_R\hat{e}_1)\exp(-\psi_R\hat{e}_3)\exp(\theta_R\hat{e}_2). \tag{2}$$

Figure 2 illustrates the physical interpretations of these angles. Moreover, its time-derivative is $\dot{Q}_R = Q_R\hat{\Omega}_R$ for $\Omega_R \in \mathbb{R}^3$ resolved in the right wing frame.

Similarly, the attitude of the left wing can be decomposed as,

$$Q_L = \exp(\beta\hat{e}_2)\exp(-\phi_L\hat{e}_1)\exp(\psi_L\hat{e}_3)\exp(\theta_L\hat{e}_2), \tag{3}$$

along with $\dot{Q}_L = Q_L\hat{\Omega}_L$ for $\Omega_L \in \mathbb{R}^3$.

The frame attached to the abdomen $\mathcal{F}_A = \{\mathbf{a}_x, \mathbf{a}_y, \mathbf{a}_z\}$ is connected to the main body through a spherical joint. Hence, its orientation is identical to the body when there is no relative rotation. Denote its relative attitude as $Q_A \in \mathsf{SO}(3)$ with $\dot{Q}_A = Q_A\hat{\Omega}_A$ for $\Omega_A \in \mathbb{R}^3$.

Since the motion of the flapping wing model is influenced by the wing, we parameterize the wing kinematics [36]. We describe the three components - flapping angle, the pitch angle, and the deviation angle. Let f be the flapping frequency and $T = \frac{1}{f}$ be the corresponding time period.

The flapping angle, ϕ, is parameterized by the expression,

$$\phi(t) = \frac{\phi_m}{\sin^{-1}\phi_K} \sin^{-1}(\phi_K \cos(2\pi f t)) + \phi_0, \tag{4}$$

where ϕ_m is the amplitude, ϕ_0 is the offset, and $0 < \phi_K \leq 1$ characterizes shape of the waveform ($\phi_K \to 0$ implies sinusoidal; $\phi_K \to 1$ implies triangular). Considering the above expression along with the physical interpretation in Figure 2(a), we observe that when $0 \leq t \leq \frac{T}{2}$ upstroke occurs and when $\frac{T}{2} \leq t \leq T$ downstroke occurs.

The pitch angle, θ, is parameterized by the expression,

$$\theta(t) = \frac{\theta_m}{\tanh\theta_C} \tanh(\theta_C \sin(2\pi f t + \theta_a)) + \theta_0, \tag{5}$$

where θ_m is the amplitude, θ_0 is the offset, $\theta_C \in (0, \infty)$ characterizes shape of the waveform ($\theta_C \to 0$ implies sinusoidal; $\theta_C \to \infty$ implies step function), and $\theta_a \in (-\pi, \pi)$ is the phase offset.

The deviation angle, ψ, can be written as,

$$\psi(t) = \psi_m \cos(2\pi\psi_N f t + \psi_a) + \psi_0, \tag{6}$$

where ψ_m is the amplitude, ψ_0 is the offset, and $\psi_a \in (-\pi, \pi)$ is the phase offset. ψ_N takes the value of either 1 or 2 which represent the number of oscillations per flapping period.

Live monarch butterflies in free flight utilize both their body and the abdomen with active pitching motion (Section 2.4). Hence, in this model they are assumed to oscillate accordingly. That is, the body pitch angle is given by,

$$\theta_B(t) = \theta_{B_m} \cos(2\pi f t + \theta_{B_a}) + \theta_{B_0}, \tag{7}$$

characterized by the parameters θ_{B_m}, θ_{B_a} $\theta_{B_0} \in \mathbb{R}$, which are the amplitude, phase offset, and offset, respectively. Utilizing this, the attitude of the body can be expressed as $R(t) = \exp(\theta_B(t)\hat{e}_2)$. The relative pitch of the abdomen is described likewise,

$$\theta_A(t) = \theta_{A_m} \cos(2\pi f t + \theta_{A_a}) + \theta_{A_0}, \tag{8}$$

with $\theta_{A_m}, \theta_{A_a}, \theta_{A_0} \in \mathbb{R}$, where the subscript are the same as for the abdomen, and the corresponding relative attitude of the abdomen is given by $Q_A(t) = \exp(\theta_A(t)\hat{e}_2)$.

2.2. Blade-Element Quasi-Steady Aerodynamics Model

To obtain dynamics of the system, the wing aerodynamic forces and moments should be evaluated. Along with a quasi-steady aerodynamics assumption, the blade-element theory is utilized [37]. More explicitly, it implies that the aerodynamic force generated by an infinitesimal chord is independent of the span-wise velocity component, and that the force and moment generated are equivalent to those for steady motion at the same instantaneous velocity and angle of attack.

Only the expressions for the right wing are mentioned since similar ones can be obtained for the left wing. Consider ρ_f as the atmospheric density, and C_L, C_D as the lift and drag

coefficients, respectively. We utilize the classical experimental results [8, 38] to model the force coefficients as

$$C_L(\alpha) = 0.225 + 1.58\sin((2.13\alpha^\circ - 7.2)\frac{\pi}{180}), \tag{9}$$

$$C_D(\alpha) = 1.92 - 1.55\cos((2.04\alpha^\circ - 9.82)\frac{\pi}{180}), \tag{10}$$

where $\alpha^\circ = \alpha\frac{180}{\pi}$. The lift L_R, drag D_R, and aerodynamic moment M_R generated by the right wing are

$$\begin{aligned} L_R(r) &= \int_0^l \frac{1}{2}\rho_f U_R^2 C_L(\alpha) c\,\mathrm{sgn}(e_1^T U_R e_3^T U_R)\frac{e_2 \times U_R}{\|e_2 \times U_R\|}dr \\ &= \int_0^l \frac{1}{2}\rho_f C_L(\alpha) c\,\mathrm{sgn}(e_1^T U_R e_3^T U_R)(e_2 \times U_R)\|U_R\|dr, \end{aligned} \tag{11}$$

$$D_R(r) = -\int_0^l \frac{1}{2}\rho_f C_D(\alpha(r))c(r)\|U_R(r)\|U_R(r)dr, \tag{12}$$

$$M_R(r) = \int_0^l re_2 \times (dL_R + dD_R), \tag{13}$$

where $r \in \mathbb{R}$ is the distance between the wing root and a point on the wing along spanwise direction, $l \in \mathbb{R}$ is the wing span, $U_R \in \mathbb{R}$ is the velocity of the aerodynamic center at r, and $\alpha \in \mathbb{R}$ is the angle of attack, defined, respectively, as

$$U_R(r) = (I_{3\times3} - e_2 e_2^T)Q_R^T(R^T\dot{x} + \Omega \times \mu_R) + r(Q_R\Omega + \Omega_R) \times e_2, \tag{14}$$

$$\alpha_R(r) = \cos^{-1}(\frac{|e_1^T U_R(r)|}{\|U_R(r)\|}). \tag{15}$$

The empirical results for C_L and C_D in equations (9) and (10) were based on a fruit fly wing geometry and wing motion, whereas we model the monarch wing geometry and motion. There are two main considerations related to these differences: i) The difference in the wing shape results in a spanwise variation in the chord $c(r)$. Dickinson et al. [8] measured the lift L and drag D, which they normalized by the wing area to obtain C_L and C_D. Because of the difference in the wing shape and wing motion, we use the blade element approach to account for the spanwise variations in the aerodynamic parameters, e.g., relative velocity U_R and angle of attack α, as shown in equations (11) and (12). In fact, (11) and (12) reduce to those used by Dickinson et al. (1999), when the linear velocity and angular velocity of the body as well as the wind velocity are small compared to the wing velocity. ii) The difference in the size and motion results in a different Reynolds number. In our study, we define the Reynolds number based on wing length R and mean wingtip velocity U_{ref}, such that $Re = \rho_f U_{\mathrm{ref}} l/\mu$, where μ is the dynamic viscosity. Although there is a large difference in the Reynolds number between the fruit fly ($Re \approx 100$) and the monarch butterfly ($Re \approx 11500$) in our study, multiple previous studies utilize the aerodynamic model of Sane and Dickinson [39] or Dickinson et al. [8] to investigate the stability and control of insects, larger than fruit flies [27, 29, 40–42]. In addition, most, if not all, studies that solve Navier-Stokes equations to model a butterfly flight assume a Reynolds number that is much lower than those relevant to monarch butterflies [32, 43–45].

Additionally, the monarchs have both fore- and hindwings, flapping in unison. Therefore, we consider the fore- and hindwings as a unified wing coupled together. This approach was used in literature for butterflies [32, 46, 46] and bees [47].

When the flapping frequency is sufficiently large, or equivalently when Ω_R is relatively large compared with other terms, it can be simply approximated by $U_R(r) \approx r\Omega_R \times e_2$, which is often used for relatively fast flapping insect models, e.g. flies or bees. However, the flapping frequency of a butterfly is about 10 Hz, where the contribution of the flapping to U_R is comparable to other terms caused by the body velocity. These expressions include spanwise variations of aerodynamic parameters like relative velocity and angle of attack, which are essential for accurate estimation corresponding to low frequency flapping of large wings.

The projected surface area of the abdomen as well as the velocity magnitude of the abdominal motion are much smaller than those of the wings. The aerodynamic forces are proportional to the wing area and velocity magnitude squared. Therefore, the aerodynamic forces generated by the abdomen are much smaller than those by the wings. Since the aerodynamic forces on the abdomen are insignificant compared to the forces on the wings, their contribution to aerodynamic forces and moments is neglected [48].

2.3. Geometric Formulation of Flapping Wing Dynamics

The dynamics of the proposed flapping wing model is formulated by Lagrangian mechanics on a manifold [49]. A single configuration of the system consists of $g = (x, R, Q_R, Q_L, Q_A)$ which evolves on the Lie group $\mathsf{G} = \mathbb{R}^3 \times \mathsf{SO(3)}^4$, Its time variation is characterized by $\xi = (\dot{x}, \Omega, \Omega_R, \Omega_L, \Omega_A)$ in the Lie algebra, $\mathfrak{g} = \mathbb{R}^3 \times \mathfrak{so}(3)^4 \simeq \mathbb{R}^3 \times (\mathbb{R}^3)^4$.

Using these notations, the kinematics equations can be generalized as,

$$\dot{g} = g\xi. \tag{16}$$

Now, denote the symmetric, positive-definite inertia tensor by $\mathbf{J} : \mathsf{G} \times \mathfrak{g} \to \mathfrak{g}^*$, and define $(\mathbf{K}_g(\xi))(\cdot) : \mathsf{G} \times \mathfrak{g} \to \mathfrak{g}^*$ such that $\mathsf{T}^*_e\mathsf{L}_g \cdot \mathbf{D}_g\mathbf{J}_g(\xi) \cdot \chi = (\mathbf{K}_g(\xi))(\chi) = \mathbf{K}_g(\xi)\chi$, where T, L and $\mathbf{D}$ denote the tangential map, the left group action, and the derivative operator, respectively. Essentially, $\mathbf{K}_g(\xi)\chi$ corresponds to the directional derivative of $\mathbf{J}_g$ when g is varied along the direction $g\chi$.

Considering $U : \mathsf{SO(3)} \to \mathbb{R}$ as the potential field, define a Lagrangian $L : \mathsf{G} \times \mathfrak{g} \to \mathbb{R}$ as $L(g, \xi) = \frac{1}{2}\langle \mathbf{J}_g(\xi), \xi \rangle - U(g)$. From which, Euler–Lagrange equations can be formulated as [49],

$$\mathbf{J}_g(\dot{\xi}) + \mathbf{K}_g(\xi)\xi - \mathrm{ad}^*_\xi \cdot \mathbf{J}_g(\xi) - \frac{1}{2}\mathbf{K}^*_g(\xi)\xi + \mathsf{T}^*_e\mathsf{L}_g\mathbf{D}_gU(g) = \mathbf{f}, \tag{17}$$

where $\mathbf{f} \in \mathbb{R}^{15}$ includes aerodynamic forces and internal torques. Here, moments acting on each of the three joints (wings and abdomen) control the dynamics. The detailed expressions for all the components involved can be found in the online supplementary material.

To simplify the mathematical analysis and the results obtained, it is assumed that attitude of the wings, abdomen, and body are prescribed, i.e., $(R(t), Q_R(t), Q_L(t), Q_A(t))$ are considered as control variables determined as a function of time, instead of toques acting on the joint. Let $m \in \mathbb{R}$ be the total mass of the vehicle, $\mathrm{g} \in \mathbb{R}$ be the acceleration due to gravity and $F_i = L_i + D_i \in \mathbb{R}^3$ be the net aerodynamic force generated by each sub-part. Under the assumption, the position dynamics are simplified into

$$m\ddot{x} + \sum_{i\in\{R,L,A\}} \left\{\mathbf{J}_{i_{12}}\dot{\Omega} + \mathbf{J}_{i_{13}}\dot{\Omega}_i + \mathbf{K}_{i_{12}}\Omega + \mathbf{K}_{i_{13}}\Omega_i\right\} = R \sum_{i\in\{R,L,A\}} Q_iF_i + mge_3. \tag{18}$$

This equation simply prescribes the evolution of vehicle position under the influence of coupling between various parts, and external forces and moments ($F_A = 0$ as mentioned in the previous sub-section). Then using (17) the control torques acting on the joints, (τ_R, τ_L, τ_A), can be reconstructed.

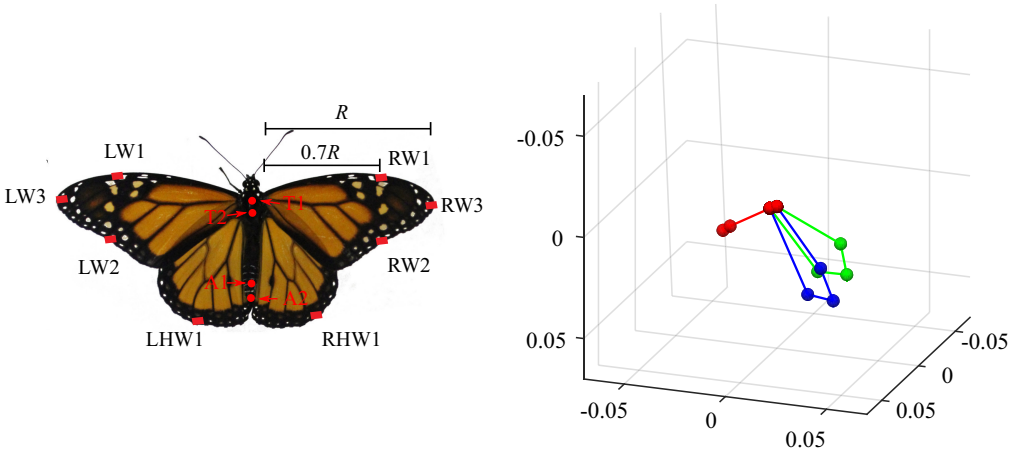

(a) Marker locations

(b) Monarch object reconstructed by markers

Figure 3. Monarch motion capture.

2.4. Comparison to Experimental Measurements of Freely Flying Monarchs

This dynamic model has been compared against the flight of live monarch butterfly acquired by a motion capture system, following a well-documented procedure [24]. We attached twelve customized reflective markers to a monarch as illustrated in Figure 3(a). The position of each marker is measured by a VICON motion capture system at 200 Hz. As illustrated in Figure 5(b), the actual flight trajectory is a slightly curved climbing. But, we analyze the gathered data by assuming that it is a straight path in the subsequent development.

The time histories of marker positions are converted into (x, R, Q_R, Q_L, Q_A) as follows. We let the origin of the body be at the center of T_1 and T_2. For the body attitude R, we assume that the first axis is along $T_1 - T_2$ and the second axis is parallel to the ground, i.e., there is no body roll. This is reasonable as the measured flight trajectory is almost straight. For the attitude of the abdomen, the first axis points from the center of A_1 and A_2 toward T_2, and the second axis is parallel to the ground. The resulting rotation matrix is left multiplied by R^T to obtain the relative attitude Q_A.

For the right wing attitude, we assume the wing root is located at the center of T_1 and T_2. The wing plane always passes through the wing root exactly, and it is spanned by the three markers on the right wing. However, due to the measurement errors and the flexibility of the wing, those points did not exactly lie on a single plane. Instead, we find the normal vector of the plane such that the sum of the squared distance between each marker and the plane is minimized. The normal vector yields the third axis of $\mathcal{F}_R$. For the second axis, the vector from the wing root to RW_3 is projected on to the fitted plane. The first axis is determined by the cross product of the second axis and the third axis. These yield the rotation matrix of the right wing from the inertial frame, and by left multiplying R^T, we obtain Q_R. The attitude of the left wing, namely Q_L is constructed similarly. We find the stroke plane such that the sum of the squared distance for $Q_R(t)e_2$ and $Q_L(t)e_2$ for varying t over the experiment period is minimized.

Our results show that the right wing tip is ahead of the left wing tip (Figure 4(a)). This might have been caused by the asymmetry of the particular monarch butterfly used in the experiment, or the bias in the marker attachment. Instead of dealing with the asymmetry

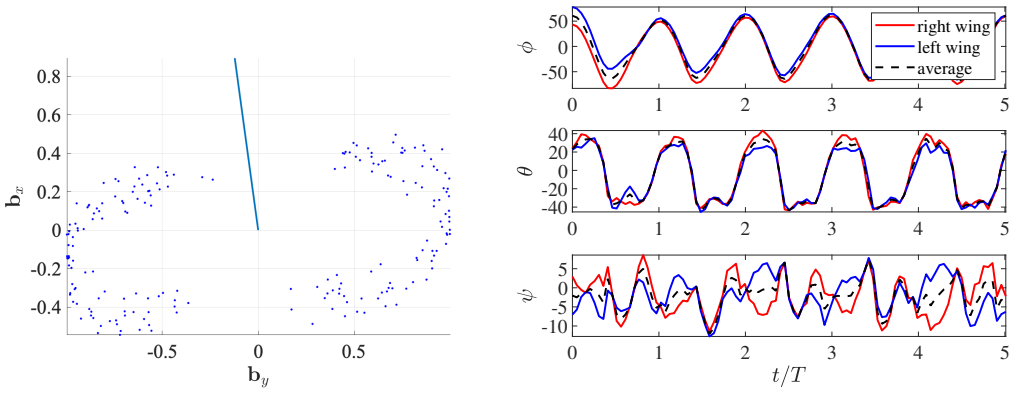

(a) Wing tip locations

(b) Wing kinematics angles

Figure 4. Monarch wing kinematics. The wing kinematics angles are in degrees.

in the left wing and the right wing, we multiply $\exp(7.77\frac{\pi}{180}\hat{e}_3)$ to Q_R and Q_L such that they become symmetric in the least square sense. The resulting stroke plane angle is $\beta = 25.42$ deg. From the given β, and rotated $Q_R(t), Q_L(t)$, we can determine the wing kinematics angles $(\phi_R(t), \theta_R(t), \psi_R(t)$, and $(\phi_L(t), \theta_L(t), \psi_L(t))$ according to equations (2) and (3), respectively. These are illustrated in Figure 4. The wing kinematics angles for the right wing are mostly consistent with the left wing, except the small deviation angle. Assuming the symmetric wing kinematics, we take the average between the right wing and the left wing and fitted with Fourier series to be used in the subsequent dynamic simulations. The frequency of oscillation experimentally measured is $f_n = 10.2\,\text{Hz}$.

From the above wing kinematics angles and the body/abdomen attitude obtained by the actual monarch butterfly, we numerically integrate the quasi-steady position dynamics, namely equation (18). The corresponding results are compared against the experimental data. These are illustrated in Figure 5. In general, the downstrokes generate the lift upward, and the upstrokes generate thrust forward, while yielding a climbing trajectory with oscillation.

The proposed quasi-steady aerodynamic model generates greater lift and thrust, and consequently causing higher climb rate and forward velocity. However, it is consistent with the experimental data in a qualitative manner.

3. Beneficial Effects of Abdomen in Energy and Power

It has been shown that Monarch butterfly actively undulates its abdomen during flight. The geometric formulation of the dynamics presented in the above section is particularly useful to study the dynamic coupling between abdomen undulation and monarch flight. In this section, we focus on the effects of abdomen in energy and power consumption for two flight maneuvers.

We first find the wing kinematics and the abdomen undulation that yield a periodic motion of the butterfly. This is formulated as a constrained optimization problem to minimize a certain performance index representing variations of the energy and power over a period while ensuring the boundary condition for periodicity. Then, the effects of abdomen are analyzed. Two cases, namely a hovering flight and a climbing flight, are considered, but these results are readily extended to other maneuvers.

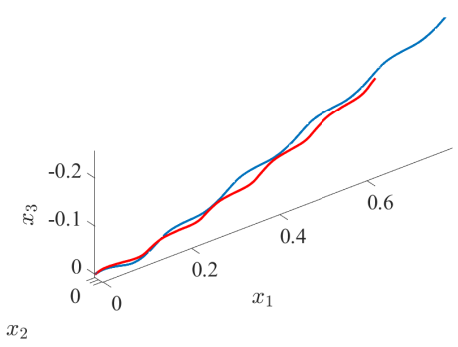

(a) Position trajectory of the body (in m)

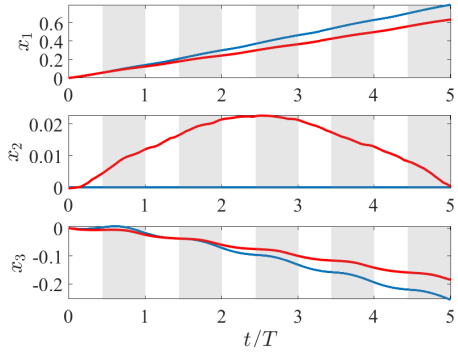

(b) Position of the body (in m)

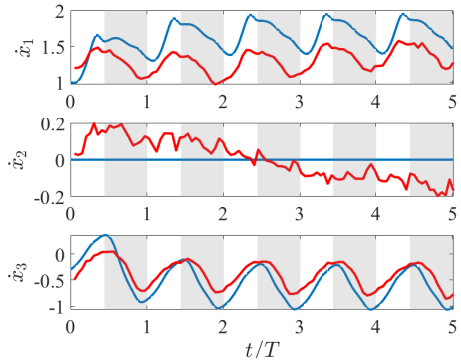

(c) Velocity of the body (in m/s)

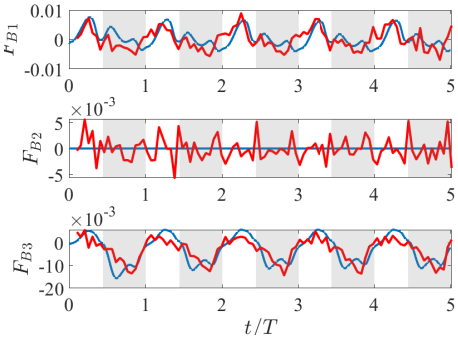

(d) Resultant force in the body-fixed frame (in N)

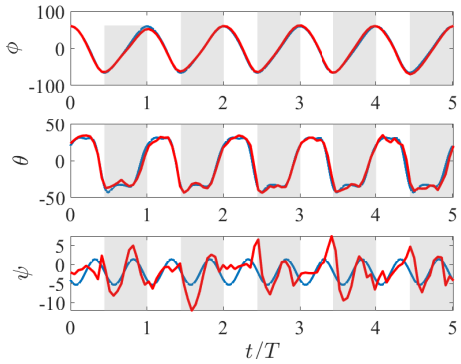

(e) Wing kinematics angles (in deg)

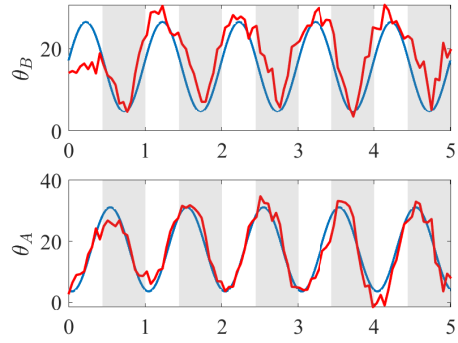

(f) Body pitch / Abdomen relative pitch (in deg)

Figure 5. Comparison between the proposed model (blue) and the experimental data (red); shaded area corresponds to downstroke; the resultant force of the experiment is constructed by the acceleration of the thorax, multiplied by the total mass and subtracted by the gravity.

3.1. Construction of Periodic Motion

The optimization problem to construct a periodic motion is formulated as follows. First, the objective function is

$$J = w_1 \int_0^T E(t)dt + w_2 \int_0^T \sqrt{\sum_{i\in\{R,L,A\}} \|\tau_i\|^2} dt, \tag{19}$$

where $w_1, w_2 \in \mathbb{R}$ are positive weighting factors, and $E(t) \in \mathbb{R}$ is the total energy of the model given by

$$E(t) = \frac{1}{2}\xi^T \mathbf{J}_g(\xi)\xi + U(t), \tag{20}$$

consisting of the kinetic energy and the gravitational potential energy. Hence, we are minimizing the average energy of the system along with a factor corresponding to average joint torques.

As the energy and the power are periodic, this essentially minimizes the variation of the energy and the power integrated over the flapping period.

The optimization parameters are composed of the wing flapping frequency, parameters that describe wing kinematics and body/abdomen undulation, and the initial velocity. More specifically, the parameters are the flapping frequency f, stroke plane angle β, flapping angle (ϕ_m, ϕ_K, ϕ_0), pitch angle $(\theta_m, \theta_C, \theta_0, \theta_a)$, deviation angle (ψ_m, ψ_0, ψ_a), body undulation $(\theta_{B_m}, \theta_{B_0}, \theta_{B_a})$, abdomen undulation $(\theta_{A_m}, \theta_{A_0}, \theta_{A_a})$, and initial velocity $\dot{x}(0)$. And ψ_N is fixed at 2 oscillations per flapping period. It is also assumed that the left wing motion is symmetric to the right wing.

Finally, the constraints enforced for periodicity are

$$x(0) = x(T) - x_f, \quad \dot{x}(0) = \dot{x}(T), \tag{21}$$

where $x_f \in \mathbb{R}^3$ is the final position to be reached after a flapping cycle. For example, $x_f = 0$ for a hovering flight. Also, there are inequality constraints imposing bounds on the optimization parameters, which are selected to ensure that the wing flapping and the body/abdomen undulation are physically feasible, $|\phi_m| + |\phi_0| < \phi_{max}$.

We consider two cases of periodic motion, namely hovering around a particular point and a forward climbing trajectory. Further, to study the effects of the abdomen, we solve an additional optimization for each case, assuming that the abdomen is fixed to the body, i.e., $\theta_A(t) = \theta_{A_0}$ and compare the resulting energy and power consumption. The corresponding optimization problems are numerically solved using global optimization tools, namely 'MultiStart' in MATLAB ‡. Here, various local minimum problems are solved with multiple start points to get an estimate of the global minimum. For all the simulations in this paper, each local minimum problem is tackled using 'fmincon' with the 'interior-point' algorithm. The parameters are constrained by the imposed bounds (see Table 1) along with nonlinear constraints like $|\phi_m| + |\phi_0| < \phi_{max}$.

3.2. Hovering Flight

To hover at a particular point, the position attained at the end of a flapping cycle should be identical to the initial value, i.e., $x_f = x(0) = [0, 0, 0]^T \mathrm{m}$ in (21). The parameters obtained after optimization for this maneuver are enlisted in the second column of Table 1.

‡ https://github.com/fdcl-gwu/FWUAV/tree/insects_exp/matlab

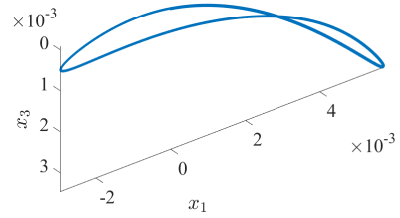

(a) x, position trajectory of the body (in m)

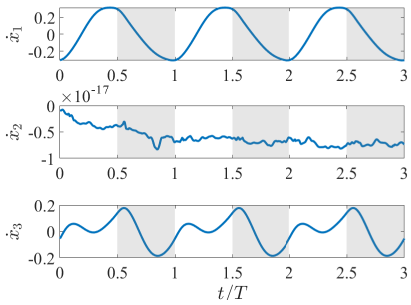

(b) $\dot{x}$, velocity of the body (in m/s)

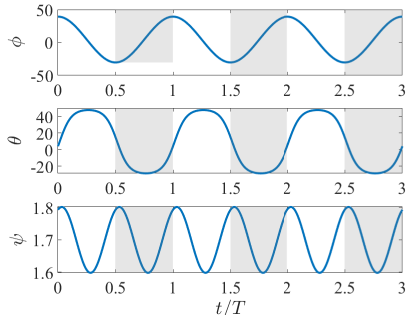

(c) Wing kinematics angles (ϕ, θ, ψ) (in deg)

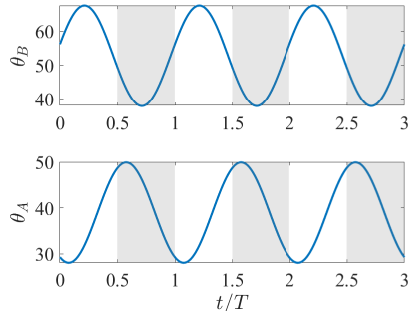

(d) Body/relative abdomen pitch θ_B, θ_A (in deg)

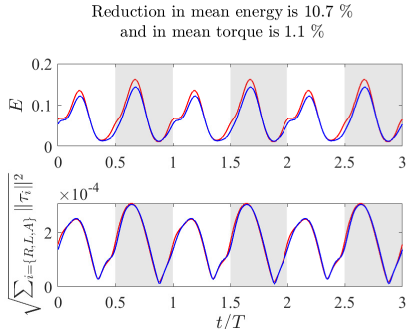

(e) Energy (in J) and torque (in Nm) comparison

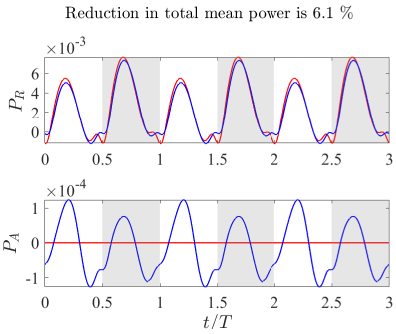

(f) Power comparison (in W)

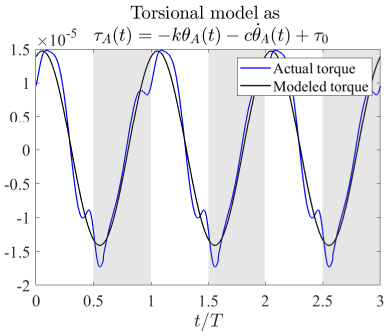

(g) Modeled torque (in Nm) with abdomen flapping

Figure 6. Hovering flight: (a)-(d) flight trajectory with abdomen undulation generated using optimized parameters, shaded region corresponds to downstrokes; (e)-(f) comparison between motion with abdomen undulation (blue) and without abdomen undulation (red).

Table 1. Parameters obtained through optimization with weights in (19) as $w_1 = 1 \times 10^4, w_2 = 1 \times 10^3$; also the natural frequency experimentally observed is $f_n = 10.2\,\mathrm{Hz}$, maximum flapping angle is taken to be $\phi_{max} = 5\pi/12$; specified data is for cases with and without abdomen undulation for both hovering and forward climbing; all angles are in radians.

Parameters			Hovering undulation		Forward climbing	
	Lower bound	Upper bound	With abdomen	Without abdomen	With abdomen	Without abdomen
$f(\mathrm{Hz})$	$0.85f_n$	$1.15f_n$	11.7220	11.6431	8.6954	8.7149
β	$-\pi/8$	$\pi/5$	0.3057	0.3240	0.0492	0.1420
ϕ_m	0	$\pi/2$	0.6073	0.6217	1.0151	1.0184
ϕ_K	0	1	0.3077	0.3073	0.4013	0.5747
ϕ_0	$-\pi/3$	$\pi/36$	0.0780	0.0566	0.0112	-0.0002
θ_m	0	$4\pi/18$	0.6657	0.6617	0.3154	0.3073
θ_C	0	3	1.4382	1.5745	1.4456	1.2895
θ_0	$-\pi/6$	$\pi/6$	0.1642	0.1437	-0.1078	-0.1207
θ_a	$-\pi/2$	$\pi/2$	-0.0896	0.0621	0.2665	0.3782
ψ_m	0	$\pi/36$	0.0018	0.0233	0.0043	0.0130
ψ_N	——	——	2	2	2	2
ψ_a	$-\pi$	π	-0.4165	0.1970	-0.9208	-1.5263
ψ_0	$-\pi/36$	$\pi/36$	0.0297	0.0000	-0.0064	-0.0008
θ_{B_m}	0	$\pi/12$	0.2582	0.2371	0.2565	0.2390
θ_{B_0}	$\pi/12$	$\pi/3$	0.9212	0.9350	0.7090	0.6061
θ_{B_a}	$-\pi/2$	$-5\pi/12$	-1.3364	-1.4701	-1.4722	-1.4775
θ_{A_m}	0	$\pi/12$	0.1905	——	0.1265	——
θ_{A_0}	$-\pi/12$	$\pi/4$	0.6806	0.6182	0.6465	0.5993
θ_{A_a}	$-7\pi/6$	$-\pi$	-3.6186	——	-3.3923	——
$\dot{x}_1(0)\ (\mathrm{m/s})$	-2	2	-0.3069	-0.3256	1.1993	1.1928
$\dot{x}_2(0)\ (\mathrm{m/s})$	-2	2	0.0000	0.0000	0.0000	0.0000
$\dot{x}_3(0)\ (\mathrm{m/s})$	-2	2	-0.0543	-0.0359	-0.9058	-0.9322
J	——	——	0.0298	0.0313	0.5870	0.5899

The corresponding states are illustrated at Figure 6(a-d). In particular, there is about 90 deg phase lag in the abdomen pitch angle, compared with the body pitch. More specifically, the body pitch is almost synchronous to the wing flapping: the pitch angle increases over the upstroke and it decreases over the downstroke. Due to the phase lag, the pitch angle of the abdomen relative to the body is minimized over the upstroke, and it is maximized over the downstroke. In order words, the tip of the abdomen bends more towards the head in the middle of the downstroke as seen in Figure 7(g).

The third column of Table 1 shows a fictitious case when there is no abdomen undulation for comparison. After the periodic motion is obtained, (17) is used to reconstruct the torques required at the joints (τ_R, τ_L, τ_A). The corresponding power at the joints are evaluated as $P_R = \tau_R^T(Q_R\Omega_R)$, $P_A = \tau_A^T(Q_A\Omega_A)$. When abdomen undulation is included, there is a 10.7% reduction in mean energy (Figure 6(e)) and a 6.1% reduction in total mean power (Figure 6(f)) with a slightly lower torque input (Figure 6(e)). The optimal value of the

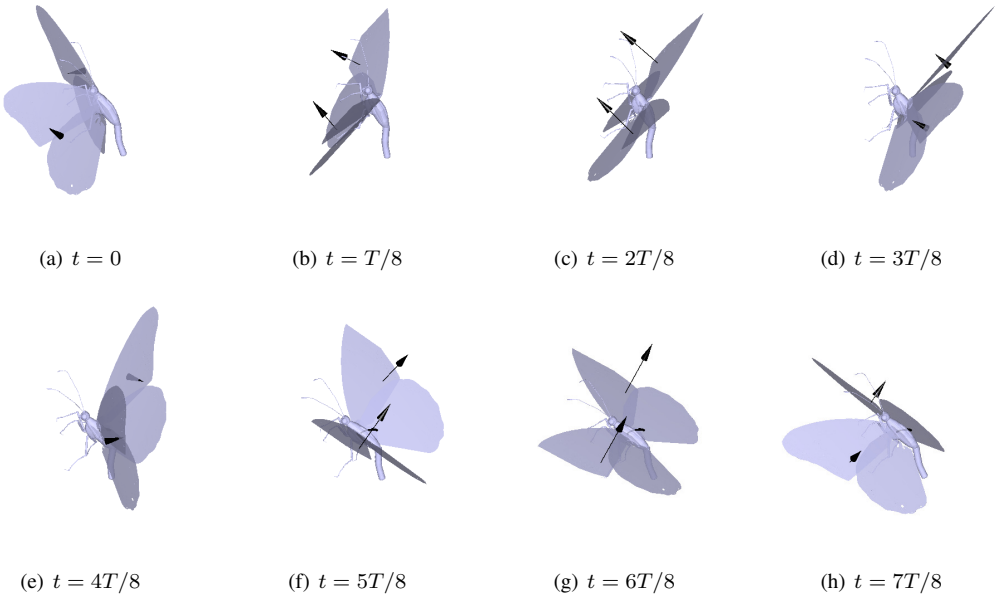

(a) $t = 0$ (b) $t = T/8$ (c) $t = 2T/8$ (d) $t = 3T/8$

(e) $t = 4T/8$ (f) $t = 5T/8$ (g) $t = 6T/8$ (h) $t = 7T/8$

Figure 7. Snapshots of flapping maneuver for hovering: (a)-(e) correspond to the upstroke; (e)-(h) and then back to (a) correspond to the downstroke; the resultant aerodynamic force at each instance is illustrated by black arrows.

objective function decreases as a result. These illustrate the beneficial effects of abdomen undulation in the energy and the power consumption.

Next, we test the question if the presented optimal abdomen undulation can be achieved in a passive way. So the hypothesis is that all the beneficial effects that are shown in the paper can be obtained without actively controlling the abdomen. Hence, we express the torque at the joint between the abdomen and the body as the torque generated by a torsional spring-damper system. More specifically, we consider the non-zero component of the abdomen torque which is along the 2nd axis ($\tau_{A_2} = \tau_A \cdot e_2 \in \mathbb{R}$) and model it as $\tau_{A_2}(t) = -k\theta_A(t) - \tilde{c}\dot{\theta}_A(t) + \tau_0$ for fixed constants $k, \tilde{c}, \tau_0$. Using a least squares fit for the data, we obtain $k = 7.5026 \times 10^{-5}$ N m rad^{-1}, $\tilde{c} = 1.3595 \times 10^{-7}$ N m s rad^{-1}, $\tau_0 = 5.1370 \times 10^{-5}$ N m. Figure 6(g) illustrates that there is a good agreement between the actual abdomen torque and the spring-damper model. This suggests the possibility of achieving the beneficial effects with passive abdomen undulation excited by the coupling with the wing flapping and the body motion.

3.3. Forward-climbing Flight

For the forward-climbing trajectory, we consider the position attained at the end of a cycle to be, $x_f = [0.1654,\ 0,\ -0.0626]^T$m. This value is motivated by the experimental results shown in Section 2.4. The parameters obtained after optimization for this maneuver are enlisted at the 4th column of Table 1, and the corresponding states are illustrated at Figure 8(a-d). The resulting flapping motion is illustrated in Figure 9 as well. Also, the additional case without abdomen undulation (5th column of Table 1) is presented with the variation of E, $\dot{E}$ and power.

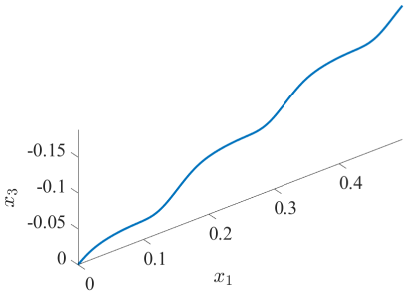

(a) x, position trajectory of the body (in m)

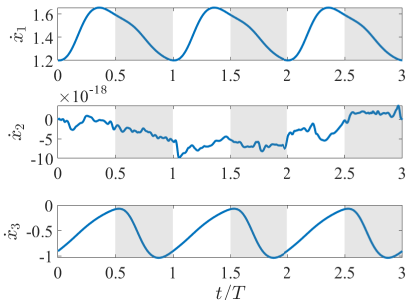

(b) $\dot{x}$, velocity of the body (in m/s)

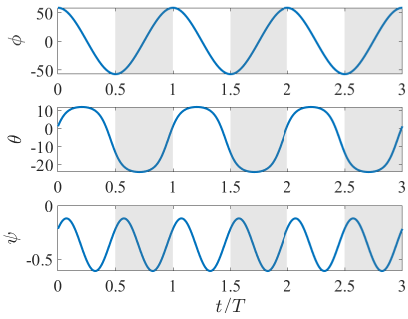

(c) Wing kinematics angles (ϕ, θ, ψ) (in deg)

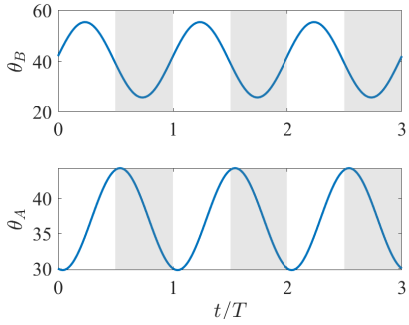

(d) Body/relative abdomen pitch θ_B, θ_A (in deg)

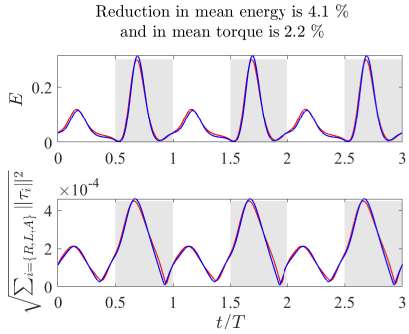

(e) Energy (in J) and torque (in Nm) comparison

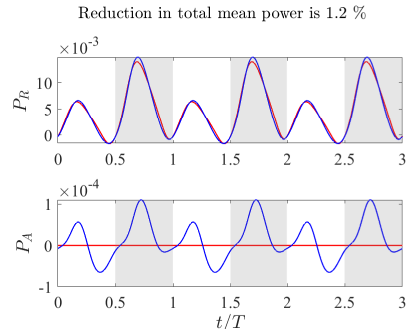

(f) Power comparison (in W)

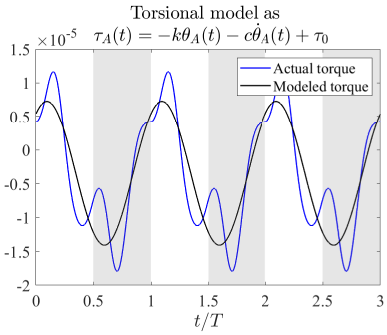

(g) Modeled torque (in Nm) with abdomen flapping

Figure 8. Forward climbing orbit with abdomen undulation generated using optimized parameters, shaded region corresponds to downstrokes; and comparison between motion with abdomen undulation (blue) and without abdomen undulation (red).

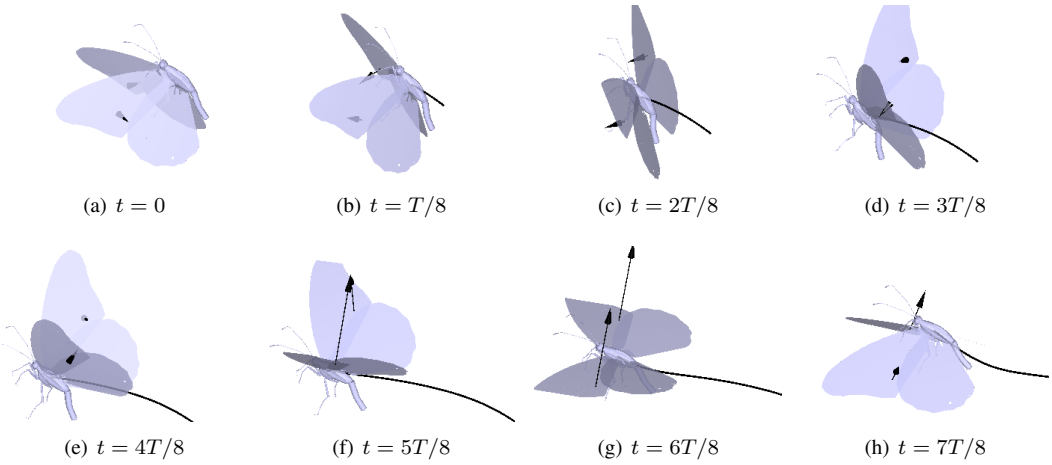

(a) $t = 0$ (b) $t = T/8$ (c) $t = 2T/8$ (d) $t = 3T/8$

(e) $t = 4T/8$ (f) $t = 5T/8$ (g) $t = 6T/8$ (h) $t = 7T/8$

Figure 9. Snapshots of flapping maneuver for forward-climbing; (e)-(h) and then back to (a) correspond to the downstroke; the resultant aerodynamic force at each instance is illustrated by black arrows.

Similar to the hovering flight, when abdomen undulation is included, there is a 4.1% reduction in mean energy (Figure 8(e)) and a 1.2% reduction in total mean power (Figure 8(f)) along with a 2.2% reduction in torque input (Figure 8(e)). For the spring-damper model of the abdomen torque, we obtain $k = 7.9354 \times 10^{-5}$ N m rad^{-1}, $\tilde{c} = -5.2353 \times 10^{-7}$ N m s rad^{-1}, $\tau_0 = 4.7894 \times 10^{-5}$ N m (Figure 8(g)).

4. Beneficial Effects of Abdomen Undulation in Stability

Now that desired trajectories have been obtained through optimization, we study the stability properties of each periodic orbit, as well as the effects of the abdomen. This is achieved using Floquet stability theory for periodic orbits.

4.1. Floquet Stability

Let the trajectory of the position dynamics (18) obtained after optimization in the previous section be denoted by $(x_d(t), \dot{x}_d(t)) \in \mathbb{R}^6$. When x_f in equation (21) is non-zero, $x_d(t)$ is not periodic. As such, we introduce a shifted position $\tilde{x}_d(t) = x_d(t) - (t/T)x_f$, which is periodic by construction. Let $\mathbf{x}_d(t) = (\tilde{x}_d(t), \dot{x}_d(t)) \in \mathbb{R}^6$ be the concatenation of the shifted position and the velocity, which satisfies $\mathbf{x}_d(t+T) = \mathbf{x}_d(t)$ for any $t > 0$. The objective of this section is studying the stability properties of the periodic orbit $\mathbf{x}_d(t)$.

Let $x(t)$ be a solution of the given dynamic model perturbed from $\mathbf{x}_d$. Also, let $\mathbf{x} = (\tilde{x}, \dot{x}) \in \mathbb{R}^6$ with $\tilde{x}(t) = x(t) - (t/T)x_f$. The resulting perturbation from the desired periodic trajectory is denoted by $\delta\mathbf{x} = \mathbf{x} - \mathbf{x}_d = (\delta\tilde{x}, \delta\dot{x}) \in \mathbb{R}^6$. By linearizing the dynamics in (18) about the desired trajectory, evolution of the perturbation variable over time is obtained as

$$\frac{d(\delta\tilde{x})}{dt} = \delta\dot{x}, \tag{22}$$

$$m\frac{d(\delta\dot{x})}{dt} = R(t)\{Q_R(t)\delta F_R(t, \delta\dot{x}(t)) + Q_L(t)\delta F_L(t, \delta\dot{x}(t))\}, \tag{23}$$

where $R(t), Q_R(t), Q_L(t)$ are values obtained from the periodic orbit, and $\delta F_R, \delta F_L$ are the variation of corresponding forces due to velocity perturbation. For instance, for the right wing,

$$\delta F_R = \delta L_R + \delta D_R, \tag{24}$$

which is evaluated using (11), (12) wherein,

$$\begin{aligned}
\delta U_R(r) &= (I_{3\times 3} - e_2 e_2^T) Q_R^T R^T \delta \dot{x}, \\
\delta \alpha_R(r) &= \frac{-1}{\sin(\alpha_R(r))} \mathrm{sgn}(e_1^T U_R(r)) \times e_1^T \left(I_{3\times 3} - \frac{U_R(r) U_R^T(r)}{\|U_R(r)\|^2} \right) \frac{\delta U_R(r)}{\|U_R(r)\|}, \\
\delta C_L(\alpha(r)) &= 1.58 \cos((2.13\alpha^\circ - 7.2)\frac{\pi}{180}) \times 2.13\ \delta\alpha_R(r), \\
\delta C_D(\alpha(r)) &= 1.55 \sin((2.04\alpha^\circ - 9.82)\frac{\pi}{180}) \times 2.04\ \delta\alpha_R(r).
\end{aligned}$$

Using the above expressions, the linearized equations corresponding to perturbation dynamics (22), (23) can be expressed as

$$\delta \dot{\mathbf{x}} = \mathbf{A}(t) \delta \mathbf{x}, \tag{25}$$

where $\mathbf{A}(t) \in \mathbb{R}^{6\times 6}$ is a periodic matrix with T as the period, i.e., $A(t+T) = A(t),\ \forall t \geq 0$. Even though $\delta \mathbf{x}(t)$ might not be periodic, it can be decomposed into a combination of periodic solutions with time varying multipliers [35]. Let the solution of the matrix differential equation $\dot{\Psi} = \mathbf{A}\Psi$ starting from any invertible $\Psi(0) \in \mathbb{R}^{6\times 6}$ be $\Psi(t) \in \mathbb{R}^{6\times 6}$. This solution is called as the *fundamental matrix* of (25). It can be determined that $\Psi(t+T) = \Psi(t)\mathbf{M},\ \forall t \geq 0$ where $\mathbf{M} \in \mathbb{R}^{6\times 6}$ is called the *monodromy matrix* [35, Chapter 3.5]. One of the simplest ways to compute the monodromy matrix is $\mathbf{M} = \Psi^{-1}(0)\Psi(T)$ starting with $\Psi(0) = \epsilon I_{6\times 6}$ where $\epsilon \in \mathbb{R}$ is a very small number characterizing the magnitude of perturbation.

The eigenvalues of the monodromy matrix, ρ_i, corresponding to the eigenvectors $\mathbf{v}_i \in \mathbb{R}^6$, are called the *characteristic multipliers* of the periodic ODE. Let $\delta \mathbf{x}_i(t) \in \mathbb{R}^6$ be the solution of the system starting from $\delta \mathbf{x}(0) = \mathbf{v}_i$, i.e., $\delta \mathbf{x}_i(t) = \Psi(t)\mathbf{v}_i$. Then,

$$\delta \mathbf{x}_i(t+T) = \Psi(t+T)\mathbf{v}_i = \Psi(t)\mathbf{M}\mathbf{v}_i = \rho_i \Psi(t)\mathbf{v}_i = \rho_i \delta \mathbf{x}_i(t). \tag{26}$$

Therefore, the characteristic solution, which starts from an eigenvector of $\mathbf{M}$, is scaled by the corresponding multiplier after each period. As the general solution which starts from any initial condition can be written as a linear combination of $\{\delta \mathbf{x}_i(t)\}_{i=1}^6$, the perturbation asymptotically converges to zero if the characteristic multipliers satisfy $|\rho_i| < 1,\ \forall i$, implying that the periodic orbit is attractive.

Furthermore, define $\mu_i \in \mathbb{R}$ such that $\rho_i = e^{\mu_i T}$, which are called the *characteristic exponents* of (25). Now let $\mathbf{p}_i(t) = \delta \mathbf{x}_i(t) e^{-\mu_i t}$ whose value after a period remains the same, $\mathbf{p}_i(t+T) = \delta \mathbf{x}_i(t+T) e^{-\mu_i t} e^{-\mu_i T} = \rho_i \delta \mathbf{x}_i(t) e^{-\mu_i t} e^{-\mu_i T} = \mathbf{p}_i(t)$. So the characteristic modes can be written as

$$\delta \mathbf{x}_i(t) = e^{\mu_i t} \mathbf{p}_i(t),$$

which implies the general solution is a combination of exponentially scaled periodic trajectories. Thus, the condition for attractivity can be restated as $\mathrm{Re}(\mu_i) < 0$ for all i. It can be observed that the characteristic properties $\mathbf{v}_i, \rho_i$ are dimensionless since $\mathbf{M}$ is dimensionless, except μ_is which can be measured in s^{-1}.

4.2. Hovering Flight

Consider the hovering flight constructed using optimization in Section 3.2. Now we numerically calculate the monodromy matrix, $\mathbf{M}$. The nontrivial characteristic modes $\delta\mathbf{x}_i$ and periodic parts $\mathbf{p}_i$ are shown in Figure 10. Also the characteristic multipliers and corresponding eigenvectors come out to be

$$\rho = \{1,\ 1,\ 1,\ 0.4869,\ 0.3343,\ 0.7921\}, \tag{27}$$

$$[\mathbf{v}_1, \ldots \mathbf{v}_6] = \begin{bmatrix} 1 & 0 & 0 & 0.0655 & -0.0742 & 0 \\ 0 & 1 & 0 & 0 & 0 & -0.3432 \\ 0 & 0 & 1 & -0.0747 & -0.0196 & 0 \\ 0 & 0 & 0 & -0.6977 & 0.9970 & 0 \\ 0 & 0 & 0 & 0 & 0 & 0.9393 \\ 0 & 0 & 0 & 0.7094 & 0.0014 & 0 \end{bmatrix},$$

while the characteristic exponents are

$$\mu = \{0,\ 0,\ 0,\ -8.4355,\ -12.8449,\ -2.7314\}\mathrm{s}^{-1}.$$

On the other hand, if we consider the case when there is no abdomen oscillation, they change into

$$\mu = \{0,\ 0,\ 0,\ -8.1835,\ -12.9912,\ -2.7176\}\mathrm{s}^{-1}.$$

Before discussing these results, we first present the results of the forward-climbing flight as follows.

4.3. Forward-climbing Flight

From the monodromy matrix of the forward-climbing flight, the characteristic multipliers and the corresponding eigenvectors are obtained to be

$$\rho = \{1,\ 1,\ 1,\ 0.4350,\ 0.1237,\ 0.2891\}, \tag{28}$$

$$[\mathbf{v}_1, \ldots \mathbf{v}_6] = \begin{bmatrix} 1 & 0 & 0 & -0.1075 & 0.0215 & 0 \\ 0 & 1 & 0 & 0 & 0 & 0.0951 \\ 0 & 0 & 1 & 0.0941 & 0.0635 & 0 \\ 0 & 0 & 0 & 0.7983 & -0.5399 & 0 \\ 0 & 0 & 0 & 0 & 0 & -0.9955 \\ 0 & 0 & 0 & -0.5851 & -0.8391 & 0 \end{bmatrix},$$

while the characteristic exponents are

$$\mu = \{0,\ 0,\ 0,\ -7.2374,\ -18.1747,\ -10.7911\}\mathrm{s}^{-1}. \tag{29}$$

The nontrivial characteristic modes are shown in Figure 11. For the other case when there is no abdomen oscillation, the characteristic exponents are

$$\mu = \{0,\ 0,\ 0,\ -6.6876,\ -19.1890,\ -11.1126\}\mathrm{s}^{-1}. \tag{30}$$

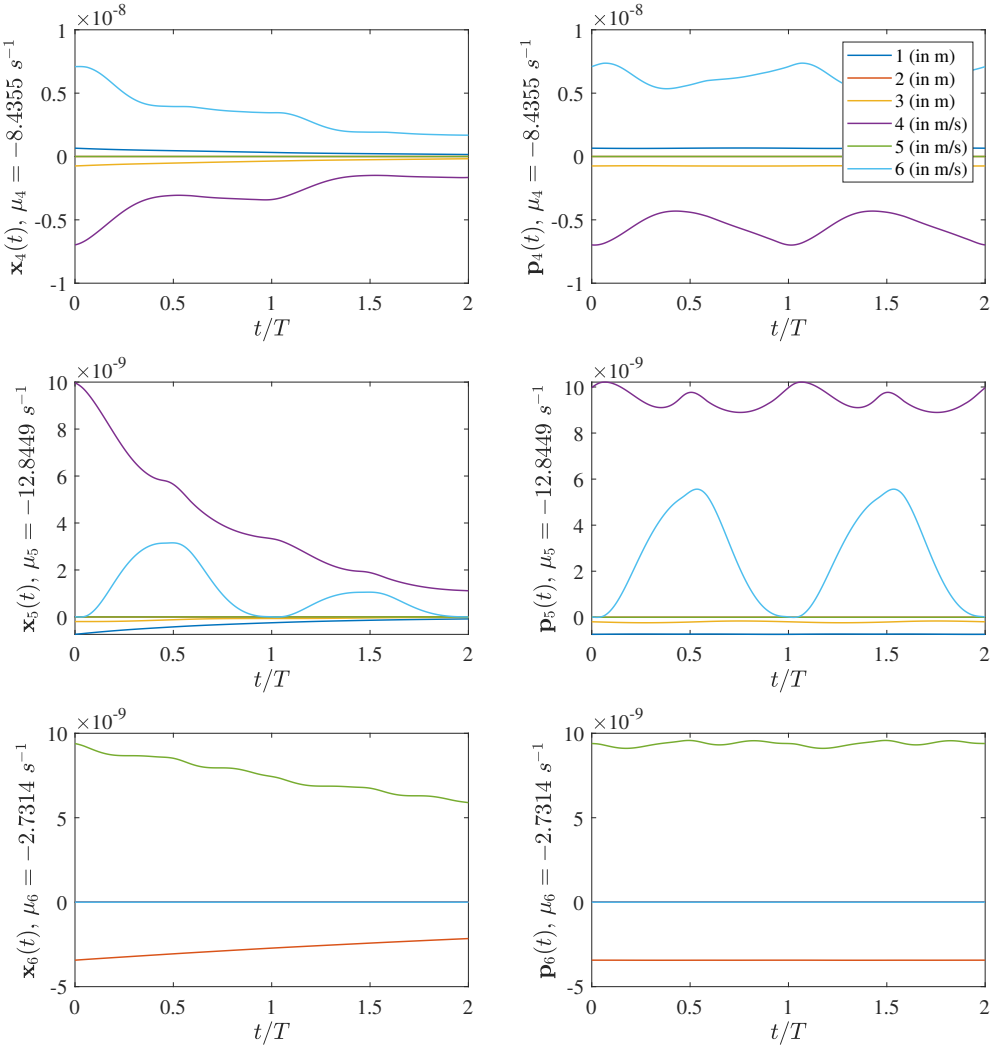

Figure 10. Characteristic modes $\delta\mathbf{x}_i$ and periodic trajectories $\mathbf{p}_i$ for $i \in \{4, 5, 6\}$ for the hover trajectory. Legend indicates the index of each component of a trajectory in $\mathbb{R}^6$ along with the corresponding unit.

4.4. Flight Stability

For both of hovering and forward climbing, the periodic orbit is stable because $|\rho_i| \leq 1$ for all i. Specifically, for the first three modes corresponding to the position perturbation, the characteristic multiplier is $\rho = 1$. This implies that when the initial position is perturbed, the periodic orbit is displaced accordingly in the three-dimensional space without altering its shape or velocity. This is not surprising as the aerodynamic forces (24) are independent of δx.

However, the velocity mode of the periodic orbit is attractive, because any initial perturbation in the velocity can be written as a linear combination of $\mathbf{v}_4, \mathbf{v}_5, \mathbf{v}_6$ whose characteristic multipliers are strictly less than 1. This can be interpreted from the fact that a velocity perturbation along a direction increases the effective angle of attack and the dynamic

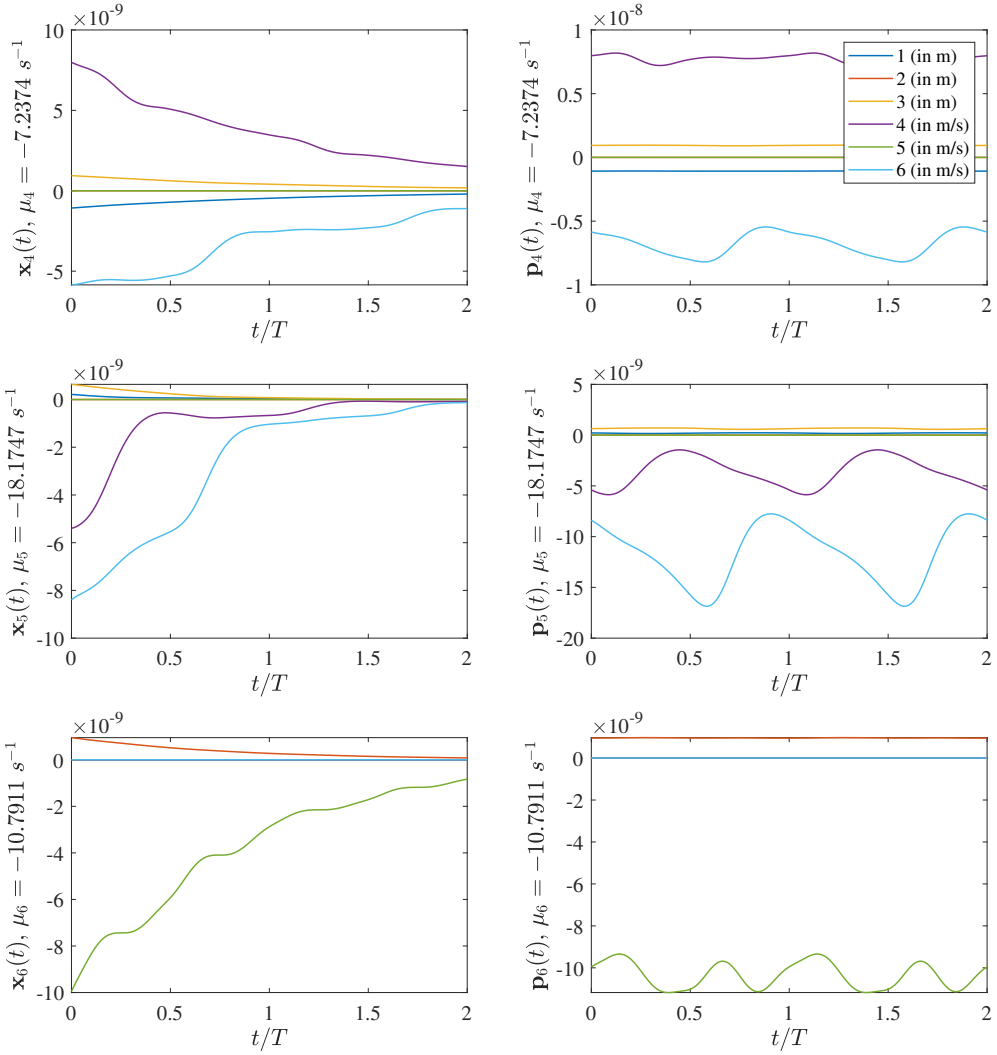

Figure 11. Characteristic modes $\delta\mathbf{x}_i$ and periodic trajectories $\mathbf{p}_i$ for $i \in \{4, 5, 6\}$ for the forward-upward trajectory. Legend indicates the index of each component of a trajectory in $\mathbb{R}^6$ along with the corresponding unit.

pressure for the aerodynamic force acting on the opposite direction, thereby generating a restoring force.

The trajectory along each of the last three modes is as follows. For both of hovering and climbing, any longitudinal velocity perturbation ($\delta\dot{x}_1 - \delta\dot{x}_3$) is spanned by the fourth and the fifth modes. And a lateral perturbation ($\delta\dot{x}_2$) is contributed by the last, sixth mode. Moreover, each mode includes the perturbation on position in the opposite direction to the velocity perturbation. For example, in the last mode of the climbing trajectory, the velocity perturbed along the negative y direction will asymptotically converge to zero, which results in a net position displacement along the negative y direction. The initial position displacement along the positive y direction will compensate it as shown at Figure 11. Besides, it can be observed that the characteristic exponents for the climbing trajectory are greater in magnitude

than the hovering case, implying it is more stable.

Finally, we analyze the effects of the abdomen undulation in stability. For hovering flight, the abdomen undulation improves the convergence rate of the fourth mode, and it makes the fifth mode slightly slower (i.e., worsens the convergence rate or decreases it in magnitude). The effects on the last lateral mode is negligible. The forward climbing shows the similar results, where the difference in the lateral mode is more significant. However, for an arbitrary velocity perturbation contributed by all of the last three modes, the overall convergence is determined by the slowest mode, as the slowest mode is what remains after the other faster and more stable modes are converged. Having stated that, it is apparent that the abdomen undulation improved the convergence rate of the slowest fourth mode: the maximum (slowest) characteristic exponent for the last three modes of the hovering flight is decreased (became faster) from $-2.7176\ \mathrm{s}^{-1}$ to $-2.7314\ \mathrm{s}^{-1}$ due to the abdomen undulation; similarly, that of the forward-climbing is reduced from $-6.6876\ \mathrm{s}^{-1}$ to $-7.2374\ \mathrm{s}^{-1}$. In short, we conclude that the abdomen undulation also improved the stability property indicated by the convergence rate of the slowest mode, or more specifically, it reduces the quantity of $\max_i\{\mu_i |\ \mu_i < 0\}$.

4.5. Stability of Monarch Butterfly Flight

Next, we analyze the stability of monarch by using the flight data reproduced by the quasi-steady dynamics presented in Section 2.4. While the flight trajectory in Figure 5 does not appear to be periodic, its velocity trajectory asymptotically converges as illustrated by Figure 12.

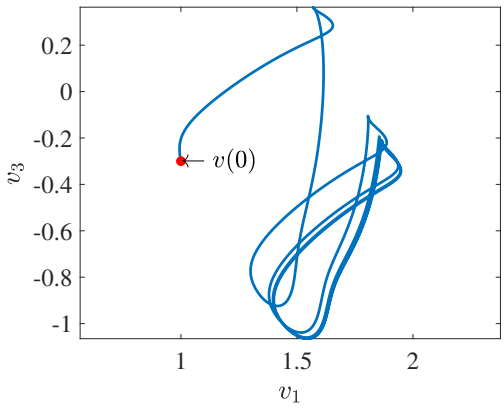

Figure 12. Velocity trajectory of the Monarch flight starting from $v(0)$ reconstructed in Section 2.4

Specifically, the trajectory becomes almost periodic after three flapping cycles. Using this trajectory after $t = 4T$ as a reference periodic orbit, we numerically obtain the fundamental solution, $\Psi(t)$, for the perturbation ODE similar to (25). Then Floquet theory can be applied to obtain a constant monodromy matrix. Specifically, starting with $\Psi(0) = \epsilon I_{6\times 6}$, we can get $\mathbf{M} = \Psi^{-1}(t)\Psi(t+T)$ for any $t \geq 4T$. Thus the nontrivial characteristic modes are shown in Figure 13 along with the *periodic* parts $\mathbf{p}_i$ which actually become periodic after

this initial time. The resulting characteristic multipliers and the eigenvectors are as follows,

$$\rho = \{1,\, 1,\, 1,\, 0.2117,\, 0.1421,\, 0.2991\},$$
$$[\mathbf{v}_1, \ldots \mathbf{v}_6] = \begin{bmatrix} 1 & 0 & 0 & -0.0562 & 0.0078 & 0 \\ 0 & 1 & 0 & 0 & 0 & -0.0950 \\ 0 & 0 & 1 & 0.0630 & -0.0760 & 0 \\ 0 & 0 & 0 & 0.7141 & 0.0162 & 0 \\ 0 & 0 & 0 & 0 & 0 & 0.9955 \\ 0 & 0 & 0 & -0.6949 & 0.9969 & 0 \end{bmatrix},$$

while the characteristic exponents are,

$$\mu = \{0,\, 0,\, 0,\, -15.8731,\, -19.9474,\, -12.3416\}\mathrm{s}^{-1}. \tag{31}$$

The stability properties are similar with those of Section 4.4 constructed by optimizing the particular wing kinematics model represented by equations (4)–(6). That said, it is intriguing to observe that the reconstructed flight of monarch has substantially smaller characteristic exponents. In other words, the wing kinematics captured from a live Monarch butterfly exhibit superior stability properties compared with the particular wing kinematics given by (4)–(6). One reason could be that the experimental data was approximated as the sum of a large number of Fourier modes whereas (4)–(6) are described by a simpler mathematical model.

4.6. Comparison with Other Insects

Finally, we study the performance and stability properties of other insects, namely hawkmoth, bumblebee, and fruitfly with varying flapping frequencies and wing sizes. We characterize these properties compared to those of the monarch butterfly. As the wing chord of such insects are not available as a function of the distance from the root, we consider a simple wing geometry assuming an elliptical wing cross-section along the chord as

$$c(r) = \frac{4\bar{c}}{\pi}\sqrt{1 - \frac{r^2}{d^2}},$$

where $\bar{c} \in \mathbb{R}$ is the mean chord length and $d \in \mathbb{R}$ is the wing base to tip distance.

The required morphological and aerodynamic parameters are listed in Table 2 for these insects. The main morphological parameters, i.e., the total mass m, wing mass m_w, wing base to tip distance d, and mean chord $\bar{c}$, follow the data as reported in Berman and Wang [36], who used experimentally measured values of fruit flies, bumblebees, and hawkmoth as reported in Sun and Du [50]. The multi-body features needed for our model are obtained by scaling the characteristics of these insects proportionate to the detailed monarch model. That is, once we have total mass of the insect, m and its wing, m_w we approximately obtain all the other parameters enumerated in the online supplementary material.

Furthermore, the lift and drag coefficients are

$$\begin{aligned} C_L(\alpha) &= C_T \sin(2\alpha), \\ C_D(\alpha) &= C_D(0)\cos^2(\alpha) + C_D(\pi/2)\sin^2(\alpha), \end{aligned}$$

where the parameters $C_T, C_D(0), C_D(\pi/2)$ were obtained by fitting empirical data [36].

Using these data, we generate wing kinematics parameters for a hovering flight by following the optimization procedure in Section 3 for each insect. The corresponding results are listed in Table 3 in comparison to the monarch. As frequency decreases and total mass

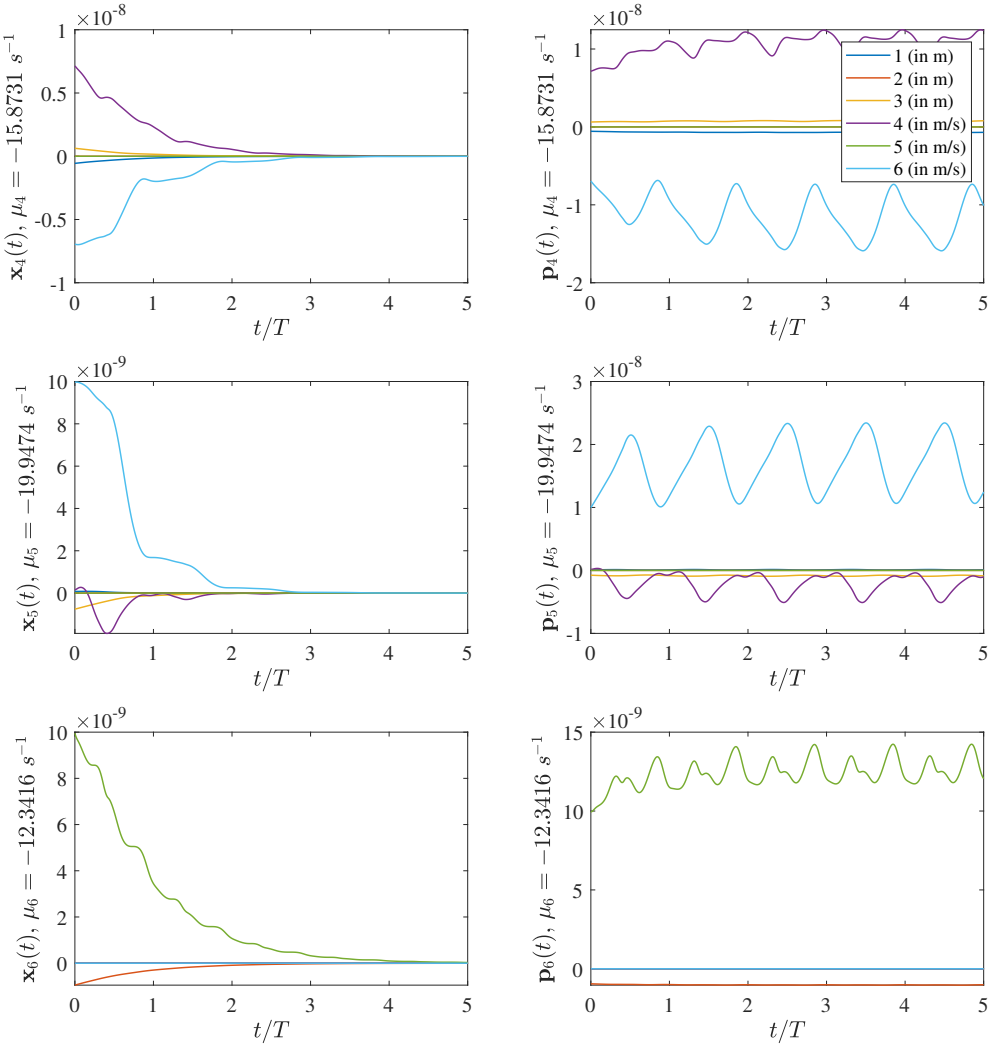

Figure 13. Characteristic modes $\delta\mathbf{x}_i$ and *periodic* trajectories $\mathbf{p}_i$ for $i \in \{4, 5, 6\}$ for the experimental trajectory. Legend indicates the index of each component of a trajectory in $\mathbb{R}^6$ along with the corresponding unit.

of the insect increases, the value of optimized J also becomes larger since it is comprised of energy and power factors.

The optimized kinematics in Table 3 are similar to experimentally observed data. For the fruit fly, the optimized flapping frequency was 285.2398 Hz, slightly higher than the observed flapping frequency range of $210 - 260$ Hz in empirical studies [36]. The flapping amplitude was 67 deg, which is within the range of measured range of $60 - 73$ deg [51]. The pitch amplitude was 37 deg, similar to the reported pitch angle at the mid-stroke of the range $20 - 55$ deg [8, 50, 52]. For the bumblebee, the optimized flapping frequency, flapping amplitude, and pitch amplitude were 126.7285 Hz (observed range: $132 - 205$ Hz [53, 54]), 72 deg (observed range: $55 - 72.5$ deg [54]), and 39 deg (observed pitch angle at mid-stroke: 28 deg [50]), respectively. For the hawkmoth, the optimized flapping frequency, flapping

Table 2. Morphological parameters of a hawkmoth, bumblebee, and fruitfly [36].

Parameters	Hawkmoth	Bumblebee	Fruitfly
f (Hz)	26.3	116	254
m(Total mass) (kg)	0.0016	1.75×10^{-4}	7.2×10^{-7}
m_w(Wing mass) (kg)	4.7×10^{-5}	4.6×10^{-7}	8.6×10^{-10}
d (m)	0.0519	0.0132	0.002
$\bar{c}$ (m)	0.0183	0.004	6.7×10^{-4}
C_T	1.678	1.341	1.833
$C_D(0)$	0.07	0	0.21
$C_D(\pi/2)$	3.06	2.93	3.35

amplitude, and pitch amplitude were 30.2343 Hz (observed range: $23 - 26.5$ Hz [55]), 47 deg (observed range: $45 - 62$ deg [55]), and 40 deg (observed pitch angle at mid-stroke range: 32 - 61 deg [50, 52]).

To understand the perturbation dynamics the equation of motion (18) is linearized to obtain (22) and (23). However, the expressions for variation in the lift and drag coefficients change to

$$\delta C_L(\alpha(r)) = 2C_T \cos(2\alpha)\, \delta\alpha_R(r)$$
$$\delta C_D(\alpha(r)) = (-C_D(0) + C_D(\pi/2)) \sin(2\alpha)\, \delta\alpha_R(r).$$

Using these values, the linearized equations can be rearranged into a periodic differential equation similar to (25). Thus we can compute the characteristic properties utilizing Floquet theory as explained in the previous section, which are summarized in Figure 14. While the flapping frequency is lowest, the monarch butterfly exhibits the faster convergence rate than the other three insects.

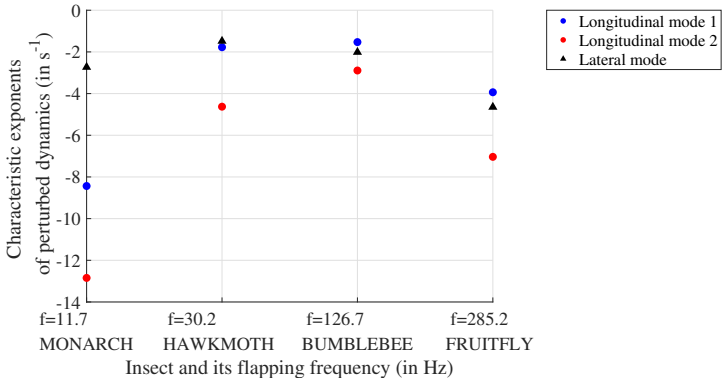

Figure 14. Stability comparison plot.

5. Concluding Remarks

This paper presents a mathematical formulation for numerical simulation, periodic orbit construction, and stability analysis of any flapping wing aerial flyer involving abdomen undulation. The dynamics of the proposed flapping wing model is formulated by Lagrangian mechanics on a manifold, composed of articulated rigid bodies such that the dynamic

Table 3. Optimized parameters for other insects. All angles are in radians.

Parameters	Monarch	Hawkmoth	Bumblebee	Fruitfly
f(Hz)	11.7220	30.2343	126.7285	285.2398
β	0.3057	0.4970	0.4137	0.4684
ϕ_m	0.6073	0.8268	1.2541	1.1613
ϕ_K	0.3077	0.2029	0.5209	0.3545
ϕ_0	0.0780	-0.0660	-0.0201	-0.0049
θ_m	0.6657	0.6977	0.6731	0.6389
θ_C	1.4382	1.7008	2.7406	2.1721
θ_0	0.1642	0.0141	0.2314	0.1191
θ_a	-0.0896	0.0851	-0.3277	-0.2280
ψ_m	0.0018	0.0742	0.0273	0.0239
ψ_N	2	2	2	2
ψ_a	-0.4165	-1.3047	0.5897	2.3759
ψ_0	0.0297	0.0000	0.0000	-0.0005
θ_{B_m}	0.2582	0.0289	0.0381	0.1424
θ_{B_0}	0.9212	1.0440	0.7324	0.9019
θ_{B_a}	-1.3364	-1.3900	-1.4296	-1.4481
θ_{A_m}	0.1905	0.0384	0.0446	0.1780
θ_{A_0}	0.6806	0.5495	0.6632	0.5951
θ_{A_a}	-3.6186	-3.6148	-3.5243	-3.4294
$\dot{x}_1(0)$ (m/s)	-0.3069	-0.1198	-0.1169	-0.1589
$\dot{x}_2(0)$ (m/s)	0.0000	0.0000	0.0000	0.0000
$\dot{x}_3(0)$ (m/s)	-0.0543	0.0061	-0.0710	-0.0775
J	0.0298	0.1282	9.436×10^{-4}	1.018×10^{-6}

effects of the inertial coupling between multiple parts can be accounted for explicitly. The wing aerodynamics is modeled using a blade element approach assuming a quasi-steady aerodynamic force and moment generation. This blade element formulation includes expressions that are essential for accurate estimation of the forces of relatively slowly flapping, large wings. Resulting trajectory and body pitch agrees reasonably well with experimental observations of monarch free flight.

The role of the abdomen motion in energy and power consumption is analyzed in hovering and forward climbing flights. Abdomen undulation in both flight modes resulted in a reduction of mean power and energy. For the hovering flight mode, the reduction in mean energy and total mean power is 10.7% and 6.1%, respectively, compared to the same trajectory without the body undulation. In forward climbing flight, these reductions are 4.1% and 1.2%, respectively.

To answer the second question if the abdomen undulation in monarch butterflies can be achieved passively, we model the torque dynamics between the body and the abdomen joint using a torsional spring-damper system. For both flight modes the spring-damper model agrees well with the actual abdomen torque. These results suggest the power benefits discussed above can be potentially achieved with passive abdomen undulation, excited by the wing-body coupling.

The effects of abdomen undulation on stability are studied using the Floquet theory. For both hovering and forward-climbing modes, the periodic orbit is attractive, providing a theoretical argument supporting the experimental observation of the stable flight of tail-less butterfly inspired ornithopter without a feedback controller [25]. Furthermore, the abdomen undulation improves the overall stability. Comparison to the stability characteristics of hawkmoth, bumblebee, and fruitfly models of varying flapping frequencies and wing sizes,

the monarch dynamics possesses the fastest convergence rate, exhibiting superior stability properties.

A beneficial role of the abdomen in insect flight, discussed in the literature, is the thrust vector redirection [34]. The presented results suggest that the abdomen may have novel desirable effects on the translational dynamics of butterfly flight, involving the total power and energy reduction and improved nonlinear stability.

For future directions, we may study the effects of abdomen undulation in the stability of the attitude dynamics. Furthermore, higher-fidelity aerodynamics model can be employed, capturing the effects of evolution of unsteady vortex dynamics and fluid-structure interaction of the wings.

Acknowledgments

This research has been supported in part by National Science Foundation (NSF) under the grants NSF CMMI-1761618 and CMMI-1760928

References

[1] Lincoln Brower. Monarch migration. *Natural History*, 85(6), 1977.

[2] L Brower. Monarch butterfly orientation: missing pieces of a magnificent puzzle. *The Journal of experimental biology*, 199:93–103, 1996. ISSN 1477-9145. URL http://www.ncbi.nlm.nih.gov/pubmed/9317405.

[3] Alan R. Masters, Stephen B. Malcolm, and Lincoln P. Brower. Monarch butterfly (danaus plexippus) thermoregulatory behavior and adaptations for overwintering in Mexico. *Ecology*, 69(2):458, apr 1988. ISSN 00129658. doi: 10.2307/1940444. URL http://www.jstor.org/stable/1940444?origin=crossref.

[4] Christine Merlin, Robert J Gegear, and Steven M Reppert. Antennal circadian clocks coordinate sun compass orientation in migratory monarch butterflies. *Science*, 325 (5948):1700–1704, sep 2009. ISSN 0036-8075. doi: 10.1126/science.1176221. URL http://www.sciencemag.org/cgi/doi/10.1126/science.1176221.

[5] D. L. Gibo. Altitudes attained by migrating monarch butterflies, Danaus P. Plexippus (Lepidoptera: Danainae), as reported by glider pilots. *Canadian Journal of Zoology*, 59: 571–572, 1981.

[6] Robert B. Srygley, Robert Dudley, Evandro G. Oliveira, and Andre J. Riveros. El Niño, host plant growth, and migratory butterfly abundance in a changing climate. *Biotropica*, 46(1):90–97, 2014. doi: 10.1111/btp.12081.

[7] R. J. Templin. Spectrum of animal flight: Insects to pterosaurs. *Progress in Aerospace Sciences*, 36(5):393–436, 2000. doi: 10.1016/S0376-0421(00)00007-5.

[8] Michael H. Dickinson, Fritz-Olaf Lehmann, and Sanjay P. Sane. Wing rotation and the aerodynamic basis of insect flight. *Science*, 284(5422):1954–1960, 6 1999. ISSN 00368075. doi: 10.1126/science.284.5422.1954. URL http://www.ncbi.nlm.nih.gov/pubmed/10373107http://www.sciencemag.org/content/284/5422/1954.short.

[9] Florian T Muijres, Michael J Elzinga, Johan M Melis, and Michael H Dickinson. Flies evade looming targets by executing rapid visually directed banked turns. *Science*, 344(6180):172–177, apr 2014. ISSN 0036-8075. doi: 10.1126/science.1248955. URL http://www.sciencemag.org/content/344/6180/172.abstracthttp://www.sciencemag.org/cgi/doi/10.1126/science.1248955.

[10] Michael E Dillon and Robert Dudley. Surpassing Mt. Everest: extreme flight performance of alpine bumble-bees. *Biology letters*, 10:20130922, 2014. ISSN 1744-957X. doi: 10.1098/rsbl.2013.0922. URL http://www.ncbi.nlm.nih.gov/pubmed/24501268.

[11] Andrew M. Mountcastle and Stacey A. Combes. Wing flexibility enhances load-lifting capacity in bumblebees. *Proceedings of the Royal Society B*, 280(1759):20130531–20130531, mar 2013. ISSN 0962-8452. doi: 10.1098/rspb.2013.0531. URL http://rspb.royalsocietypublishing.org/cgi/doi/10.1098/rspb.2013.0531.

[12] Z. Jane Wang. Dissecting insect flight. *Annual Review of Fluid Mechanics*, 37(1):183–210, jan 2005. doi: 10.1146/annurev.fluid.36.050802.121940. URL http://arjournals.annualreviews.org/doi/abs/10.1146/annurev.fluid.36.050802.121940.

[13] S. R. Jongerius and D. Lentink. Structural analysis of a dragonfly wing. *Experimental Mechanics*, 50(9):1323–1334, oct 2010. ISSN 0014-4851. doi: 10.1007/s11340-010-9411-x.

[14] Z.J. Wang. High-order methods for the Euler and Navier–Stokes equations on unstructured grids. *Progress in Aerospace Sciences*, 43(1-3):1–41, jan 2007. doi: 10.1016/j.paerosci.2007.05.001.

[15] D.E. E. Alexander. Unusual phase relationships between the forewings and hindwings in flying dragonflies. *Journal of Experimental Biology*, 109(1):379–383, 1984.

[16] J. K. Wang and Mao Sun. A computational study of the aerodynamics and forewing-hindwing interaction of a model dragonfly in forward flight. *Journal of Experimental Biology*, 208(19):3785–3804, oct 2005. doi: 10.1242/jeb.01852.

[17] Wei Shyy, Hikaru Aono, Chang-kwon Kang, and Hao Liu. *An Introduction to Flapping Wing Aerodynamics*. Cambridge University Press, New York, New York, 2013.

[18] C R Betts and R J Wootton. Wing shape and flight behaviour in butterflies (lepidoptera: Papilionoidea and hesperioidea): A preliminary analysis. *Journal of Experimental Biology*, 138(1):271–288, 1988. ISSN 0022-0949, 1477-9145. URL http://jeb.biologists.org/content/138/1/271.abstract.

[19] R Dudley. Biomechanics of flight in neotropical butterflies: aerodynamics and mechanical power requirements. *Journal of experimental biology*, 357(1):335–357, 1991. ISSN 00220949. URL http://jeb.biologists.org/content/159/1/335.short.

[20] A. L. R. Thomas, G. K. Taylor, R. B. Srygley, R. L. Nudds, and Richard J. Bomphrey. Dragonfly flight: free-flight and tethered flow visualizations reveal a diverse array of unsteady lift-generating mechanisms, controlled primarily via angle of attack. *Journal of Experimental Biology*, 207(24):4299–4323, nov 2004. doi: 10.1242/jeb.01262.

[21] Robert B Srygley. Locomotor mimicry in butterflies? the associations of positions of centres of mass among groups of mimetic, unprofitable prey. *Philosophical Transactions of the Royal Society of London B: Biological Sciences*, 343(1304):145–155, jan 1994.

[22] R Dudley and R Srygley. Flight physiology of neotropical butterflies: Allometry of airspeeds during natural free flight. *The Journal of experimental biology*, 191(1):125–39, 1994. ISSN 1477-9145. URL http://jeb.biologists.org/content/191/1/125.long.

[23] T Lin, L Zheng, T Hedrick, and R Mittal. The significance of moment-of-inertia variation in flight manoeuvres of butterflies. *Bioinspiration & Biomimetics*, 7(4):044002, 2012. ISSN 1748-3182. doi: 10.1088/1748-3182/7/4/044002.

[24] Chang-kwon Kang, Jacob Cranford, Madhu K. Sridhar, Deepa Kodali, David Brian Landrum, and Nathan Slegers. Experimental characterization of a butterfly in climbing flight. *AIAA Journal*, 56(1):15–24, 2018. doi: 10.2514/1.j055360.

[25] Hiroto Tanaka and Isao Shimoyama. Forward flight of swallowtail butterfly with simple flapping motion. *Bioinspiration & biomimetics*, 5(2):026003, 2010. doi: 10.1088/1748-3182/5/3/039801.

[26] M. J. Elzinga, F. van Breugel, and M. H. Dickinson. Strategies for the stabilization of longitudinal forward flapping flight revealed using a dynamically-scaled robotic fly. *Bioinspiration & biomimetics*, 9:025001, 2015.

[27] Haithem E. Taha, Muhammad R. Hajj, and Ali H. Nayfeh. Flight dynamics and control of flapping-wing MAVs: a review. *Nonlinear Dynamics*, 70(2):907–939, jul 2012. doi: 10.1007/s11071-012-0529-5.

[28] Luca Schenato. *Analysis and control of flapping flight: from biological to robotic insects*. Phd dissertation, University of California, Berkeley, 2003.

[29] Xinyan Deng, L. Schenato, Wei Chung Wu, S.S. Sastry, X. Deng, L. Schenato, W. C. Wu, and S.S. Sastry. Flapping flight for biomimetic robotic insects: part I-system modeling. *IEEE Transactions on Robotics*, 22(4):776–788, aug 2006. doi: 10.1109/TRO.2006.875480.

[30] David B. Doman, Michael W. Oppenheimer, and David O. Sigthorsson. Wingbeat shape modulation for flapping-wing micro-air-vehicle control during hover. *Journal of Guidance, Control, and Dynamics*, 33(3):724–739, may 2010. ISSN 0731-5090. doi: 10.2514/1.47146. URL http://arc.aiaa.org/doi/abs/10.2514/1.47146.

[31] Wei Shyy, Chang-kwon Kang, Pakpong Chirarattananon, Sridhar Ravi, and Hao Liu. Aerodynamics, sensing and control of insect-scale flapping-wing flight. *Proceedings of the Royal Society A: Mathematical, Physical and Engineering Science*, 472(2186): 20150712, feb 2016. ISSN 1364-5021. doi: 10.1098/rspa.2015.0712.

[32] Naoto Yokoyama, Kei Senda, Makoto Iima, and Norio Hirai. Aerodynamic forces and vortical structures in flapping butterfly's forward flight. *Physics of Fluids*, 25(2):021902, 2013. doi: 10.1063/1.4790882.

[33] Jeeva Jayakumar, Kei Senda, and Naoto Yokoyama. Control of pitch attitude by abdomen during forward flight of two-dimensional butterfly. *Journal of Aircraft*, 55 (6):2327–2337, nov 2018. doi: 10.2514/1.c034767.

[34] Jonathan P Dyhr, Kristi A Morgansen, Thomas L Daniel, and Noah J Cowan. Flexible strategies for flight control: an active role for the abdomen. *Journal of Experimental Biology*, 216(9):1523–1536, 2013.

[35] Gerald Teschl. *Ordinary differential equations and dynamical systems*, volume 140. American Mathematical Soc., 2012.

[36] Gordon J Berman and Z Jane Wang. Energy-minimizing kinematics in hovering insect flight. *Journal of Fluid Mechanics*, 582:153–168, 2007.

[37] Charles Porter Ellington. The aerodynamics of hovering insect flight. i. the quasi-steady analysis. *Philosophical Transactions of the Royal Society of London. B, Biological Sciences*, 305(1122):1–15, 1984.

[38] Sanjay P Sane and Michael H Dickinson. The control of flight force by a flapping wing: lift and drag production. *Journal of experimental biology*, 204(15):2607–2626, 2001.

[39] Sanjay P Sane and Michael H Dickinson. The aerodynamic effects of wing rotation and a revised quasi-steady model of flapping flight. *Journal of experimental biology*, 205(8): 1087–1096, 2002.

[40] James E Bluman, Chang-kwon Kang, and Yuri Shtessel. Control of a Flapping-Wing Micro Air Vehicle: Sliding-Mode Approach. *Journal of Guidance, Control, and Dynamics*, 41(5):1219–1225, 2018. doi: 10.2514/1.G003160.

[41] Michael W. Oppenheimer, David B. Doman, and David O. Sigthorsson. Dynamics and Control of a Biomimetic Vehicle Using Biased Wingbeat Forcing Functions. *Journal of Guidance, Control, and Dynamics*, 34(1):204–217, jan 2011. doi: 10.2514/1.49735.

[42] Bo Cheng and Xinyan Deng. Translational and rotational damping of flapping flight and its dynamics and stability at hovering. *IEEE Transactions on Robotics*, 27(5):849–864, 2011. doi: 10.1109/TRO.2011.2156170.

[43] Kosuke Suzuki, Keisuke Minami, and Takaji Inamuro. Lift and thrust generation by a butterfly-like flapping wing-body model: Immersed boundary-lattice Boltzmann simulations. *Journal of Fluid Mechanics*, 767:659–695, 2015. doi: 10.1017/jfm.2015.57.

[44] K. Suzuki, I. Okada, and M. Yoshino. Effect of wing mass on the free flight of a butterfly-like model using immersed boundary-lattice Boltzmann simulations. *Journal of Fluid Mechanics*, 877:614–647, 2019. doi: 10.1017/jfm.2019.597.

[45] Kosuke Suzuki, Takaaki Aoki, and Masato Yoshino. Effect of chordwise wing flexibility on flapping flight of a butterfly model using immersed-boundary lattice Boltzmann simulations. *Physical Review E*, 100:013104, 2019. doi: 10.1103/PhysRevE.100.013104.

[46] Shigeru Sunada and K Kawachi. Performance of a Butterfly in Take-Off Flight. *Journal of Experimental Biology*, 277(183):249–277, 1993.

[47] Mao Sun and Yan Xiong. Dynamic flight stability of a hovering bumblebee. *Journal of Experimental Biology*, 208(3):447–459, 2005. doi: 10.1242/jeb.01407.

[48] Lingxiao Zheng, Tyson L. Hedrick, and Rajat Mittal. Time-Varying Wing-Twist Improves Aerodynamic Efficiency of Forward Flight in Butterflies. *PLoS One*, 8(1): e53060, jan 2013. doi: 10.1371/journal.pone.0053060.

[49] T. Lee, M. Leok, and N. H. McClamroch. *Global Formulation of Lagrangian and Hamiltonian Dynamics on Manifolds*. Springer, 2018. doi: 10.1007/978-3-319-56953-6.

[50] Mao Sun and Gang Du. Lift and power requirements of hovering insect flight. *Acta Mechanica Sinica*, 19(5):458–469, 2003. doi: 10.1007/bf02484580.

[51] Steven N Fry, Rosalyn Sayaman, and Michael H Dickinson. The Aerodynamics of Hovering Flight in Drosophila. *The Journal of Experimental Biology*, 208:2303–2318, 2005. doi: 10.1242/jeb.01612.

[52] H. Liu and H. Aono. Size effects on insect hovering aerodynamics: An integrated computational study. *Bioinspiration and Biomimetics*, 4(1), 2009. doi: 10.1088/1748-3182/4/1/015002.

[53] R Dudley and C P Ellington. Mechanics of Forward Flight In Bumblebees. I. Kinematics and Morphology. *Journal of Experimental Biology*, 148:19–52, 1990.

[54] Stacey A. Combes, Susan F. Gagliardi, Callin M. Switzer, and Michael E. Dillon. Kinematic flexibility allows bumblebees to increase energetic efficiency when carrying heavy loads. *Science Advances*, 6(6), 2020. doi: 10.1126/sciadv.aay3115.

[55] Alexander P Willmott and Charles P Ellington. The Mechanics of Flight in the Hawkmoth Manduca Sexta. I. Kinematics of Hovering and Forward Flight. *Journal of Experimental Biology*, 200:2705–2722, 1997.